7 Simulation of the deformation of polycrystals including intergranular fracture

7.1 Introduction

Ductile fracture of polycrystalline metals takes place by the propagation of a crack throughout the microstructure after significant plastic deformation. Crack propagation may take place through the grains (transgranular fracture) or along the GBs (intergranular fracture). In particular, intergranular cracking has been often identified as one of the mechanisms responsible for the reduced ductility of many metallic alloys [125] due to either microstructural or environmental effects. The former involves the segregation of impurities during solidification and/or the precipitation of brittle phases during heat treatments while GB embrittlement may be caused by liquid metal embrittlement [129], hydrogen embrittlement [21, 150], stress corrosion cracking [90, 161], and neutron irradiation [18, 49]. In all cases, the local stresses at the GB are key factors to trigger intergranular fracture, and they depend on the dislocation interaction with GBs.

The mechanisms and modeling of ductile fracture of metallic polycrystals have been extensively studied in the past, assuming that the material behaves as an elastoplastic solid following the J2 theory of plasticity [61, 177] or strain gradient plasticity models [121] but the analysis of ductile fracture at the mesoscale has not received similar attention. Frodal *et al.* [59] recently presented a crystal plasticity model to assess fracture in smooth and notched tensile specimens where each grain was explicitly modeled. Fracture was introduced using a continuum damage approach based on a damage parameter that reduces the strength of the material as damage progresses. Clayton and McDowell [42] and Alabort *et al.* [5] analyzed intergranular fracture in polycrystalline metals through the combination of crystal plasticity and cohesive elements at the grain boundaries. Both investigations confirmed that the strength and ductility of polycrystalline metals can be dramatically affected by GB damage. Furthermore, Alabort *et al.* [5] reported that GBs perpendicular to the loading axis tended to fail prematurely at strengths well below the macroscopic yield stress. Nevertheless, these simulations were carried out in 2D or in specimens containing a few grains, and the overall influence of the microstructure (grain

size, texture, etc.) on the mechanisms of GB cracking could not be analyzed. Moreover, the effect of slip blocking was not included in the crystal plasticity model.

As shown in Chapter 6, crystal plasticity can take into account the strengthening effect of GBs. Moreover, the effect of slip transfer can also be included to simulate the local stress concentration/relief induced by dislocation pile-up/transmission at GBs, leading to more realistic representations of dislocation-GB interactions. In this chapter, the effect of GB character (fully opaque, fully transparent, and translucent GBs) on the mechanisms of intergranular fracture is analyzed in polycrystalline thin foils of Al (FCC) and Mg (HCP). These two metals were selected to study the effect of plastic isotropy (FCC) versus plastic anisotropy (HCP) on fracture. The tensile response of foils with different crystal orientations and GB characteristics under different loading conditions (plane stress and plane strain) was simulated, and the effect of the GB features on fracture was assessed.

7.2 Constitutive behavior

7.2.1 Crystal plasticity model

The physically-based crystal plasticity model presented in Chapter 6 was used to simulate the behavior of the grains. The mechanical behavior of the Al (FCC) single crystals was governed by the crystal plasticity model presented in Section 6.2.1. Plastic deformation was dictated by dislocation slip along the 12 slip systems from the {111} family in Table 1.1. The viscoplastic parameters and the dislocation interaction coefficients are included in Table 6.1, and the parameters of the crystal plasticity model are referred to in Table 6.2.

The mechanical behavior of the Mg (HCP) single crystals was governed by the same physically-based crystal plasticity model presented in Section 6.2.2. A total of 12 slip systems were considered for Mg, distributed in three $<a>$ basal, three $<a>$ 4 prismatic, and six second-order $<a+c>$ pyramidal slip systems (Table 1.2). The parameters of the viscoplastic law for Mg are the same as those presented in Table 6.4. The stiffness constants for pure Mg can be found in Table 6.3, and the parameters of the dislocation-based crystal plasticity model in 6.7. Nevertheless, the matrix $q_{\alpha\beta}$ was modified to account for the interactions between dislocations on different slip systems in the hardening. Instead of the same-hardening assumption employed in Chapter 6, the latent-hardening coefficients obtained by Bertin *et al.* through dislocation dynamics simulations for Mg were used (Table 7.1).

7.2.2 Slip transfer/blocking at GBs

The behavior of GBs from the viewpoint of slip transfer (either transparent, translucent, or opaque) was taken into account through Eqs. 6.4 and 6.5 for FCC Al and Eqs. 6.9 and 6.10 for HCP Mg. To account for the effect of GBs in the numerical simulations, the distance to the nearest GB from each Gauss point needs to be calculated, as explained in Section 6.3. Then, the neighbor grain across the boundary can be identified for each slip system α at each Gauss integration point. The likelihood of slip transfer from the slip system α in

Table 7.1: Latent-hardening coefficients for the dislocation interaction matrix $q_{\alpha\beta}$ for pure Mg [23].

Interaction	Value
Basal self-interaction	0.15
Prismatic self-interaction	0.15
Pyramidal $<c+a>$ self-interaction	0.15
Coplanar basal/basal	0.15
Prismatic/prismatic	0.038
Collinear basal/prismatic	0.707
Non-collinear basal/prismatic	0.054
Collinear prismatic/basal	0.535
Non-collinear prismatic/basal	0.06
Semi-collinear basal/pyramidal $<c+a>$	0.367
Non-collinear basal/pyramidal $<c+a>$	0.293
Semi-collinear prismatic/pyramidal $<c+a>$	0.068
Non-collinear prismatic/pyramidal $<c+a>$	0.088
Semi-collinear pyramidal $<c+a>$/basal	0.017
Non-collinear pyramidal $<c+a>$/basal	0.011
Semi-collinear pyramidal $<c+a>$/prismatic	0.025
Non-collinear pyramidal $<c+a>$/prismatic	0.015
Semi-collinear pyramidal $<c+a>$/pyramidal $<c+a>$	0.018
Non-collinear pyramidal $<c+a>$/pyramidal $<c+a>$	0.042

grain A to any of the slip systems β in the neighbor grain B was assessed according to the Luster-Morris geometrical parameter m' as

$$m'_{\alpha\beta} = (\boldsymbol{n}_\alpha \cdot \boldsymbol{n}_\beta)(\boldsymbol{b}_\alpha \cdot \boldsymbol{b}_\beta) \tag{7.1}$$

where $\boldsymbol{n}_\alpha$ and $\boldsymbol{n}_\alpha$ are unit vectors perpendicular to the slip plane α in grain A and slip plane β in grain B. All the vectors involved in this calculation have to be expressed in the same reference frame, as explained in Section 6.3.

In the case of FCC metals, slip transfer between slip systems α and β is allowed when $m' > 0.8$. If the condition of slip transfer is fulfilled for any β slip system in the neighbor grain, Eq. 6.4 is used as the constitutive equation of slip system α at the Gauss integration point of the crystal. Otherwise, slip transfer from α to β is not possible due to the geometric incompatibility, and the constitutive equation is expressed by Eq. 6.5. The same strategy was for Mg (HCP), regardless of the slip system family. This means that, for instance, slip transfer will be possible for an incoming basal slip system α if $m' > 0.8$ for any outgoing β slip system, regardless of whether it is basal, prismatic, or pyramidal. If this condition is fulfilled, Eq. 6.9 would be used for the dislocation accumulation; otherwise, Eq. 6.10 is used to indicate slip blocking. It should be noted that the model is general and

allows to use of different thresholds for slip transfer for each combination of incoming and outgoing slip system families (either basal, prismatic, or pyramidal) and impedes slip transfer between two different slip system families. However, for the sake of simplicity, this possibility was not included in the simulations.

The geometrical analysis of slip transfer at each GB indicates how many pairs of slip systems are suitably oriented to transfer slip across the boundary, leading to a classification of GBs from fully opaque (slip transfer is not possible for any pair of slip systems) to translucent (slip transfer is possible for some pairs of slip systems) to fully transparent (slip transfer is allowed for all slip systems).

7.2.3 Intergranular fracture modeling

Cohesive zone modeling is a numerical technique used in the field of computational mechanics to simulate the behavior of materials, particularly in the context of fracture and delamination [50, 139]. It represents the interaction between adjacent material surfaces by defining a cohesive zone with its own material properties, such as fracture energy and stiffness. Cohesive zone modeling is widely employed in engineering and materials science to analyze and predict the behavior of materials under various loading conditions, especially in applications involving adhesive bonding, composites, and structural integrity assessments [27, 32, 111, 187].

Cohesive zone modeling can be performed through the use of either cohesive elements or cohesive surfaces [163]. The choice between cohesive elements and surfaces-based cohesive behavior depends on the specific analysis requirements and the desired balance between computational simplicity and modeling accuracy. Cohesive elements are recommended for more detailed analyses or complex constitutive behaviors at the cost of additional pre-processing effort and increased computational cost. In contrast, cohesive surfaces are computationally more efficient and accurate enough for analyses that assume negligible interface thickness. In the past, GB fracture has been modeled through the insertion of both cohesive surfaces [5, 162] and cohesive elements [159].

The cohesive zone approach [16, 46] for damage initiation and evolution is used as the constitutive law for GBs. In this context, a traction-separation law is typically used to define the relationship between the forces (traction t) and relative displacements (separation δ) between two material surfaces along the cohesive zone. The typical bilinear cohesive traction-separation law is represented in Fig. 7.1, where the behavior of the cohesive surfaces before damage is linear-elastic, and there is a linear stiffness decrease after damage initiation until the final failure. The subindices n, s, and t denote the normal and the two orthogonal shear directions in the cohesive surface. The area under the curve represents the total fracture energy of the cohesive surface G_C.

Thus, the evolution of the tractions of a cohesive surface with a bilinear traction-separation law can be mathematically described by:

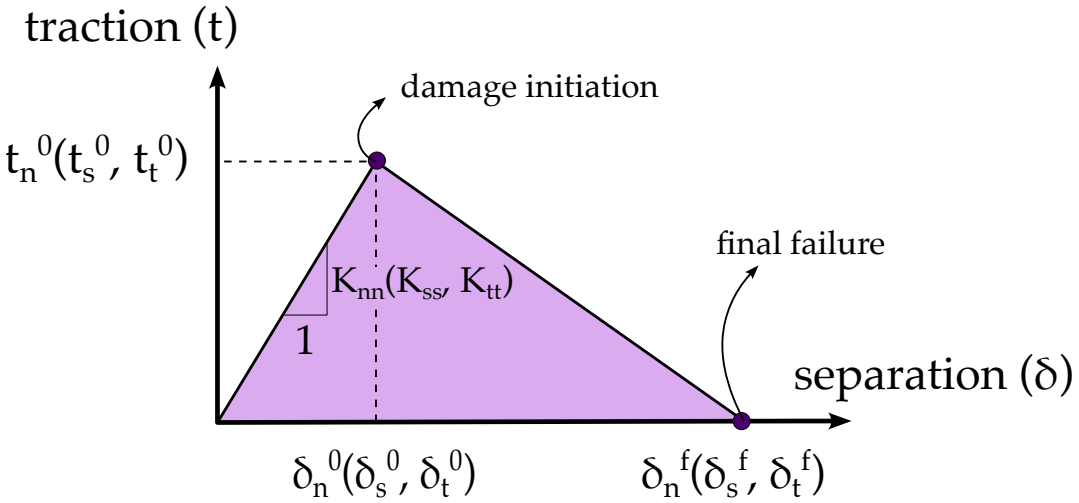

Figure 7.1: Bilinear traction-separation law, where damage initiation is indicated by the superindex 0 and failure is indicated by the superindex f.

$$\begin{Bmatrix} t_n \\ t_s \\ t_t \end{Bmatrix} = \begin{bmatrix} K_{nn}[1-D(\delta)] & 0 & 0 \\ 0 & K_{ss}[1-D(\delta)] & 0 \\ 0 & 0 & K_{tt}[1-D(\delta)] \end{bmatrix} \begin{Bmatrix} \delta_n \\ \delta_s \\ \delta_t \end{Bmatrix} \tag{7.2}$$

where K_{nn}, K_{ss}, and K_{tt} represent the stiffness constants, and δ_n and δ_s and δ_t stand for the normal opening and the two shear displacements between both cohesive surfaces, respectively. $D(\delta)$ is a scalar damage variable, which represents the overall damage in a cohesive surface. The damage evolution is typically represented by a decreasing linear stiffness law as follows:

$$D(\delta) = \begin{Bmatrix} 0; & \delta < \delta^0 \\ \dfrac{\delta^f(\delta - \delta^0)}{\delta(\delta^f - \delta^0)}; & \delta \geq \delta^0 \end{Bmatrix} \tag{7.3}$$

where δ is defined as an effective displacement, and δ_n, δ_s and δ_t stand for the separations in the different directions. The effective displacement δ was defined by Camanho *et al.* [31] as

$$\delta = \sqrt{\delta_n^2 + \delta_s^2 + \delta_t^2} \tag{7.4}$$

The damage initiation point δ^0 is defined according to the selected damage initiation law. A maximum stress criterion was selected for the damage initiation according to,

$$\text{MAX}\left\{\frac{t_n}{t_n^0}, \frac{t_s}{t_s^0}, \frac{t_t}{t_t^0}\right\}, \tag{7.5}$$

where t_n^0, t_s^0, and t_t^0 are the critical stresses that lead to the onset of damage in the cohesive surface. The damage evolution in a cohesive surface in Abaqus can be controlled by either

an energy-based or a separation-based law. A maximum separation criterion based on δ_n^f, δ_s^f, and δ_t^f was selected in this investigation.

Depending on how the user defines these six variables (critical stresses and critical displacements), the behavior of the cohesive surfaces will be more or less anisotropic. In this investigation, the behavior of the cohesive surfaces was assumed to be isotropic, and thus the stiffness, the stress for damage initiation, and the maximum separations were equally set for the three directions and depended only on two parameters, t_i^0 and δ_i^f. Damage initiation is determined by t_i^0 and the damage evolution by δ_i^f. Both parameters control the area under the traction-separation law and, hence, the total fracture energy of the cohesive surfaces. Moreover, the initial stiffness of the cohesive surfaces is set to a very large value, so the separation between the cohesive surfaces at the GB is negligible until the onset of damage.

First, the stress for damage initiation, t_i^0, was chosen for each metal (either Al or Mg) according to stresses at the GBs in a simulation without considering intergranular fracture (without cohesive surfaces) for the strongest case, which corresponds to the fully opaque GBs. Then, the maximum separation, δ_i^f, was selected to reach a fracture energy of 1.5 J/m^2 for both Al and Mg, which is a reasonable value for GB energy in metals [29, 199]. The cohesive surface interaction parameters used for Al and Mg are indicated in Table 7.2.

Table 7.2: Interaction properties for the cohesive surfaces introduced at GBs in the Al and Mg thin foils.

Material	K_{ii} [MPa]	t_i^0 [MPa]	δ_i^f [μm]	G_C [J/m^2]
Al (FCC)	$3 \cdot 10^7$	15	20	1.5
Mg (HCP)	$3 \cdot 10^7$	20	15	1.5

7.3 Numerical model

7.3.1 Finite element model

The effect of GBs on the deformation and fracture of FCC and HCP polycrystals was determined by means of the finite element simulation of pseudo-3D foils of Al (FCC) and Mg (HCP) polycrystals under uniaxial tension. Thus, the columnar GBs perpendicular to the foil were included between the grains.

The microstructures were generated using Neper [146]. The grains within the foils were generated using Laguerre-Voronoi tessellations, which lead to polyhedra with flat interfaces. The foil dimensions in the sample reference frame are shown in Fig. 7.2, where $L_x = 0.3$ mm, $L_y = 0.15$ mm, and $L_x = 0.015$ mm. In other words, $L_x = 20 \cdot L_z$, and $L_y = 10 \cdot L_z$. The notation of the boundary faces is provided on the left in Fig. 7.2, with z_0 and z_1 being the bottom and top surfaces of the foil, respectively, and x_0, x_1, y_0, and y_1 the lateral faces in the x and y directions.

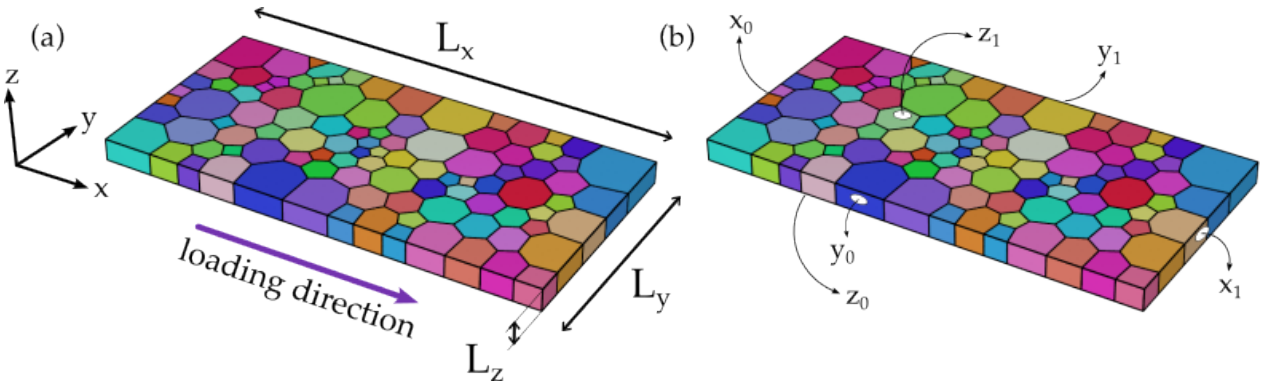

Figure 7.2: Thin foil with columnar grains to simulate the effect of GBs in FCC and HCP metals. The reference frame and the loading direction are indicated in (a), and the notation employed for the foil boundary faces is indicated in (b).

Two different realizations with 100 grains, R_1 and R_2, respectively, were generated. Microstructure R_1 is composed of 263 GBs, while R_2 includes 268 GBs. The grain size in both realizations followed a lognormal distribution with a mean grain size of 20 μm and a standard deviation of 4 μm. The grain shape was equiaxed in the xy plane and columnar along z (see reference frame in Fig. 7.3).

Three foils were employed to simulate the mechanical behavior in Al (Fig. 7.3). Foils 1 and 2 have the same grain distribution (R_1) and different random crystal orientations, whereas foil 3 has a different microstructure (R_2) as well as random crystal orientations. In contrast, four different foils were employed for the numerical simulation of Mg. The same two geometrical realizations, R_1 and R_2, were used, and two sets of crystal orientations were assigned to each of them: one with random crystal orientations and the other with a strong basal texture. This texture was obtained from X-ray diffraction of an AZ31 Mg alloy reported by Jamali *et al.* [87]. 100 representative orientations were extracted from the orientation distribution function (ODF) with MTEX [15] for R_1 and R_2, and the basal pole figure is provided in Fig. 7.4.

Once the microstructure was tessellated, it was discretized with $\approx 40k$ second-order modified tetrahedra (C3D10M elements with ten nodes in Abaqus) for the finite element simulations using Gmsh [63].

7.3.2 Cohesive surfaces

Cohesive surfaces were chosen to model intergranular fracture. This approach was chosen rather than cohesive elements for the sake of simplicity and given that no special constitutive fracture behavior is attributed to GBs. The shared nodes between the adjacent grains were duplicated, and the contact pairs between each master and slave cohesive surface were defined through an in-house Matlab code. An example of the cohesive surfaces generated in one of the thin foils is presented in Fig. 7.5. The cohesive surfaces were generated for both microstructure realizations R_1 and R_2, regardless of the crystal orientations. The constitutive behavior of the cohesive surfaces for Al and Mg is indicated in Section 7.2.3.

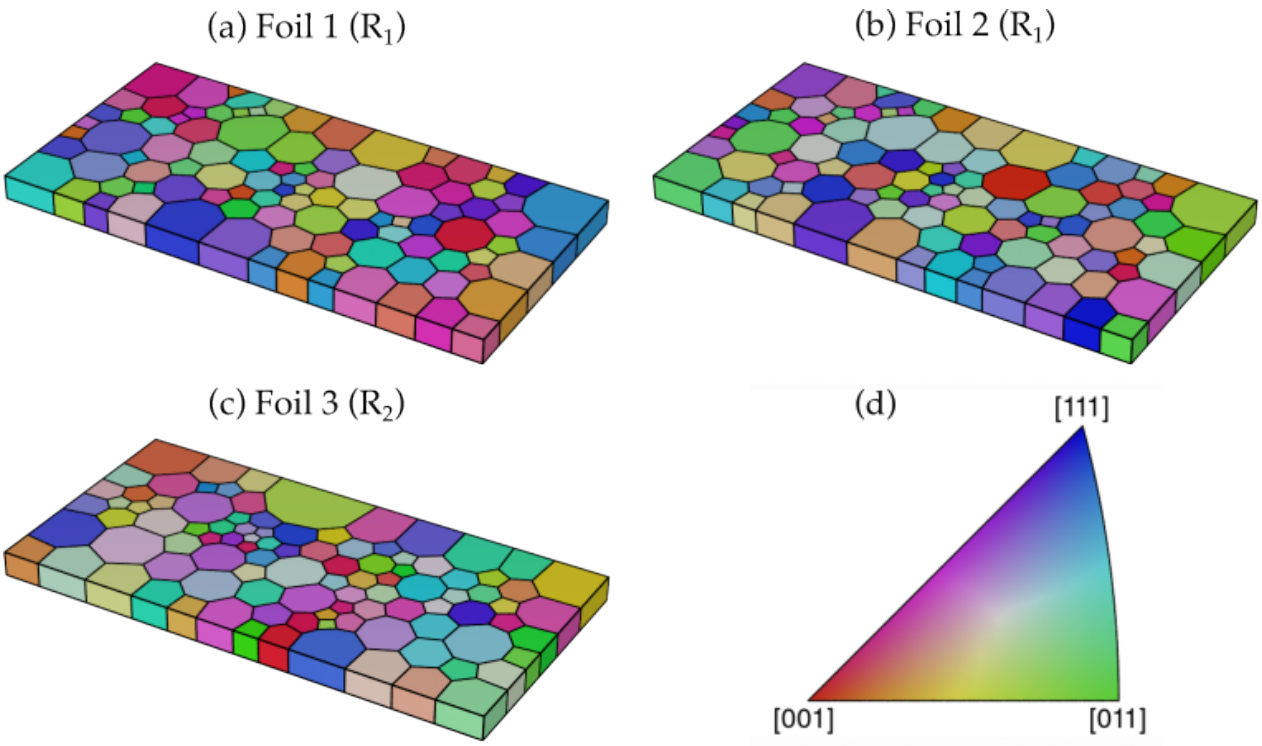

Figure 7.3: Thin foils used to simulate the effect of GBs in Al (FCC) (a)-(c). The grains within the foils are colored according to the inverse pole figure along z, provided in (d). Note that foils 1 and 2 have the same grain distribution (R_1) but different crystal orientations, while foil 3 has a different grain distribution (R_2).

7.3.3 Boundary conditions

The thin foils were subjected to uniaxial loading along the x direction. The displacements at the surface x_0 were set to 0 along the x direction while an increasing displacement was applied in the opposite face x_1 in the loading direction, which is parallel to x. The thin foils were deformed up to 5% under a quasi-static strain rate of 10^{-3} s^{-1}. The stresses on the lateral surfaces, given by $y = y_0$ and y_1, were 0 to simulate uniaxial tension along x.

Two different loading scenarios were considered: plane stress and plane strain. In the plane stress condition, the stresses on the bottom (z_0) and top (z_1) surfaces were set to 0, leading to an approximation of the stress state on the surface of the polycrystal. In a plane strain condition, the out-of-plane displacements along the z axis are restricted and set to 0. This stress state is a (crude) approximation of the stress state within the bulk of the polycrystal under uniaxial loading when the displacements perpendicular to the loading axis are hindered by the neighbor grains.

Three different GB characters were employed for each foil: fully opaque GBs, fully transparent GBs, and translucent GBs, where slip transfer is allowed when $m' > 0.8$ between any family of slip systems. Hence, twelve simulations were carried out for each foil, six including intergranular fracture and six without intergranular fracture. Three GB characters and the two loading conditions were carried out for each foil with or without intergranu-

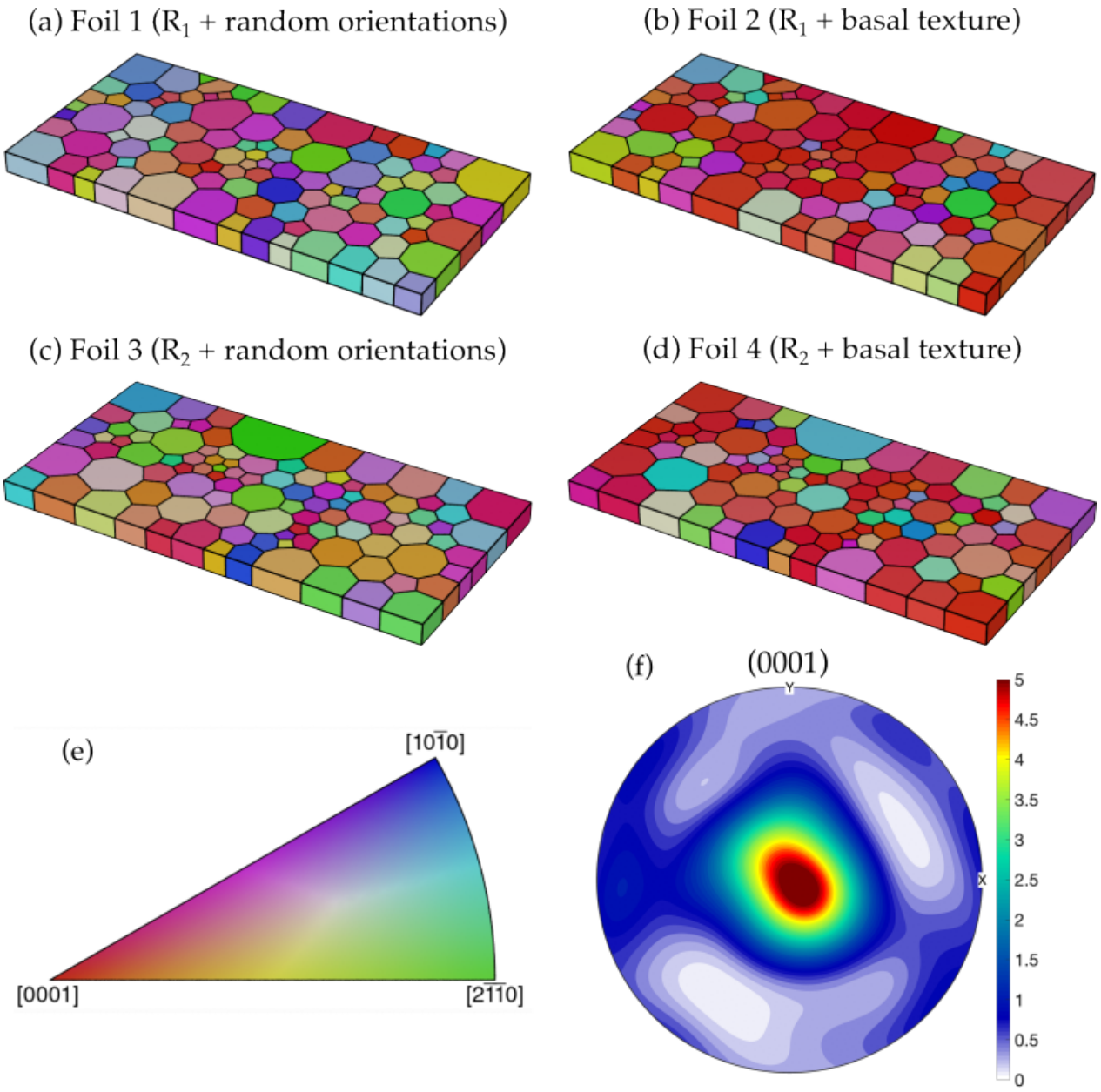

Figure 7.4: Thin foils used to simulate the effect of GBs in Mg (HCP) (a)-(d). The grains within the foils are colored according to the inverse pole figure along z, provided in (e). Note that two different grain realizations were generated (R_1 and R_2), and two different sets of crystal orientations were used for each foil: random orientation and a strong basal texture. The basal pole figure for the microstructures with basal texture is shown in (f).

lar fracture.

The mechanical behavior of the foils under uniaxial tension was simulated using Abaqus Standard [163] within the framework of the finite deformations theory with the initial unstressed state as reference. The crystal plasticity models were implemented in Abaqus through a user-defined material model (UMAT).

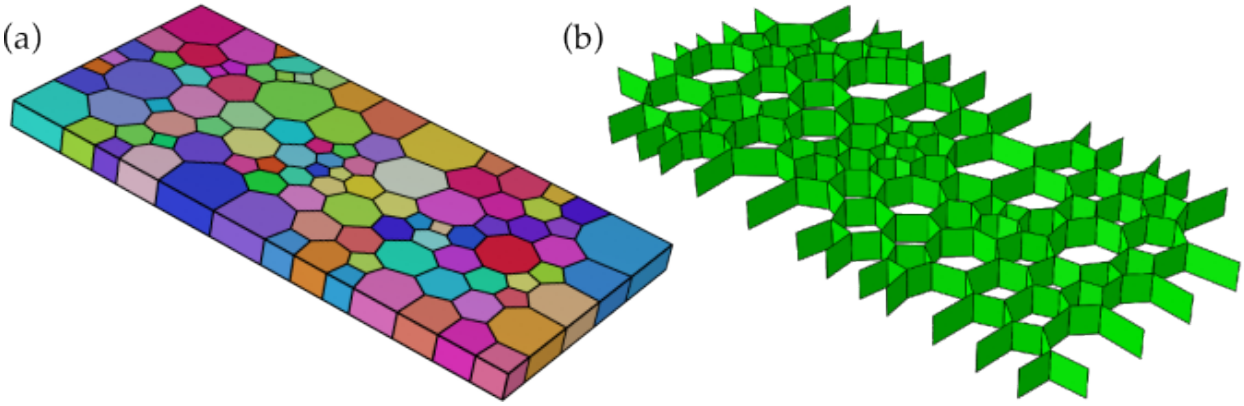

Figure 7.5: Example of thin foil polycrystal (left), together with the sample reference frame and loading direction, and cohesive surfaces generated at the GBs of the same polycrystal (right).

7.4 GB damage analysis

The effect of different GB features on damage nucleation and propagation was analyzed from the results of the numerical simulations, including cohesive surfaces. Different GB characteristics were considered for the analysis, namely geometrical and crystallographic. Regarding the geometrical factors, the GB length $\mathrm{L_{GB}}$ and the angle between the GB and the loading axis α_x ($0 < \alpha_x < 90°$) were included. From the crystallographic point of view, the GB misorientation angle Θ was also considered. The number of transparent slip systems per GB $\mathrm{n_{Trs}}$ was included to analyze the effect of GB character on intergranular fracture. Given that 12 slip systems were considered for both Al and Mg, $\mathrm{n_{Trs}}$ was equal to 12 for the simulations with fully transparent GBs and equal to 0 for the simulations with fully opaque GBs. The simulations with translucent GBs incorporated the Luster-Morris parameter as the slip transfer criterion, and slip transfer was allowed for an incoming slip system as long as there was at least one outgoing slip system with $m' > 0.8$. In that case, such incoming slip system would be considered transparent. Thus, $\mathrm{n_{Trs}}$ could range from 0 to 12 per GB for the simulations with translucent GBs.

An additional parameter named the slip activation factor SA was defined in order to account for the probability of each grain to deform along a certain slip system family. This parameter depends on the Schmid factors of the possible active slip systems in the family according to

$$\mathrm{SA}_{ss} = \frac{\sum_{i=1}^{n_{ss}} \mathrm{SF}_i}{n_{ss} \cdot \mathrm{SF}_{max}}, \tag{7.6}$$

where n_{ss} is the number of slip systems in the family considered, SF_i is the Schmid factor of each slip system i, and SF_{max} is the maximum value that the Schmid factor can take, which is 0.5. Thus, the slip activation factor gives a measure of how well the slip systems of a certain family are oriented to generate dislocation slip. In the case of Al (FCC), there is only one family of {111} slip systems. Thus, the number of slip systems n_{ss} is equal to

12, and there is only SA per grain. In contrast, three different slip activation factors can be determined in Mg (HCP). They are SA_b, SA_p, and SA_{py}, which stand for the corresponding slip activation factors for basal, prismatic, and second-order pyramidal slip. The different values of n_{ss} per slip system family (three for basal, three for prismatic, and six for pyramidal slip) are considered to calculate the respective slip activation factors.

The variables $\mathrm{L_{GB}}$, α_x, Θ, and $\mathrm{n_{Trs}}$ are related to the GB while the slip activation factor SA is linked to the grain. The connection of SA with a GB was carried out through the arithmetic mean of the SA of the grains across the GB. In the case of Mg (HCP), three SA were calculated for each GB, and they correspond to the arithmetic mean of the basal, prismatic, and pyramidal SA of the grains across the GB. Hence, $\overline{\mathrm{SA}}_\mathrm{b}$, for instance, would represent the arithmetic mean of the slip activation factor for basal slip in the two grains at either side of a GB while $\overline{\mathrm{SA}}_\mathrm{p}$ and $\overline{\mathrm{SA}}_\mathrm{py}$ have the same meaning for prismatic and pyramidal slip.

The strain for damage initiation ε^0_{dmg} was used as GB damage indicator. The Pearson correlation coefficient (r) was used to assess the correlation between the different GB features and ε^0_{dmg}. The Pearson correlation measures the degree of the linear relationship between two variables [99]. It ranges between -1 to 1, where a value of -1 means a total negative linear correlation, 0 means no correlation, and +1 means a total positive correlation. A schematic representation of the Pearson correlation is provided in Fig. 7.6, presenting a strong positive correlation $r > 0$ in (a), no linear correlation $r = 0$ in (b), and strong negative correlation $r < 0$ in (c).

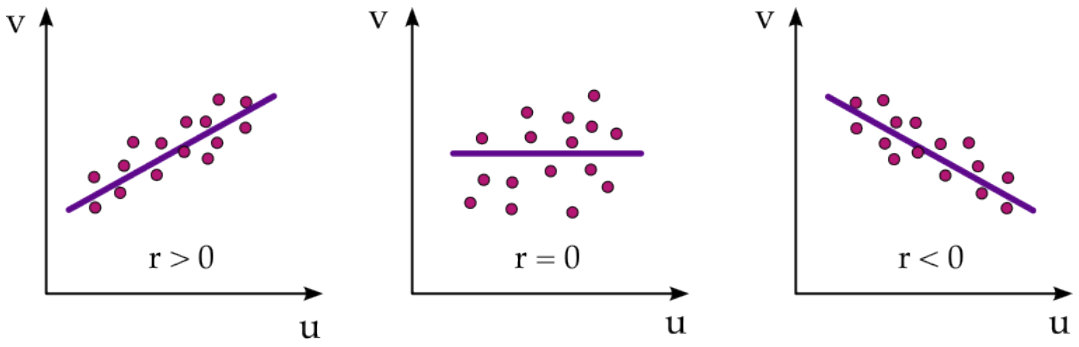

(a) Strong positive correlation (b) No correlation (c) Strong negative correlation

Figure 7.6: Schematic representation of Pearson correlation between two variables u and v: (a) strong positive correlation with $r > 0$, (b) no correlation with $r = 0$, and (c) strong negative correlation.

The Pearson correlation coefficient between two variables u and v can be mathematically expressed as

$$r(u, v) = \frac{s_{uv}}{s_u \times s_v}, \tag{7.7}$$

where s_{uv} is the covariance between the variables u and v, and s_u and s_v stand for the standard deviations of u and v, respectively [99]. This coefficient was computed to analyze

the effect of the different GB features on damage initiation ε^0_{dmg} for the different thin foils in which intergranular fracture was considered.

7.5 Results and discussion

7.5.1 Intergranular fracture of Al foils in tension

The numerical simulations of the tensile response of the three Al thin foils with and without intergranular fracture are plotted as a function of GB character under plane stress in Fig. 7.7 (a), and under plane strain in Fig. 7.7 (b).

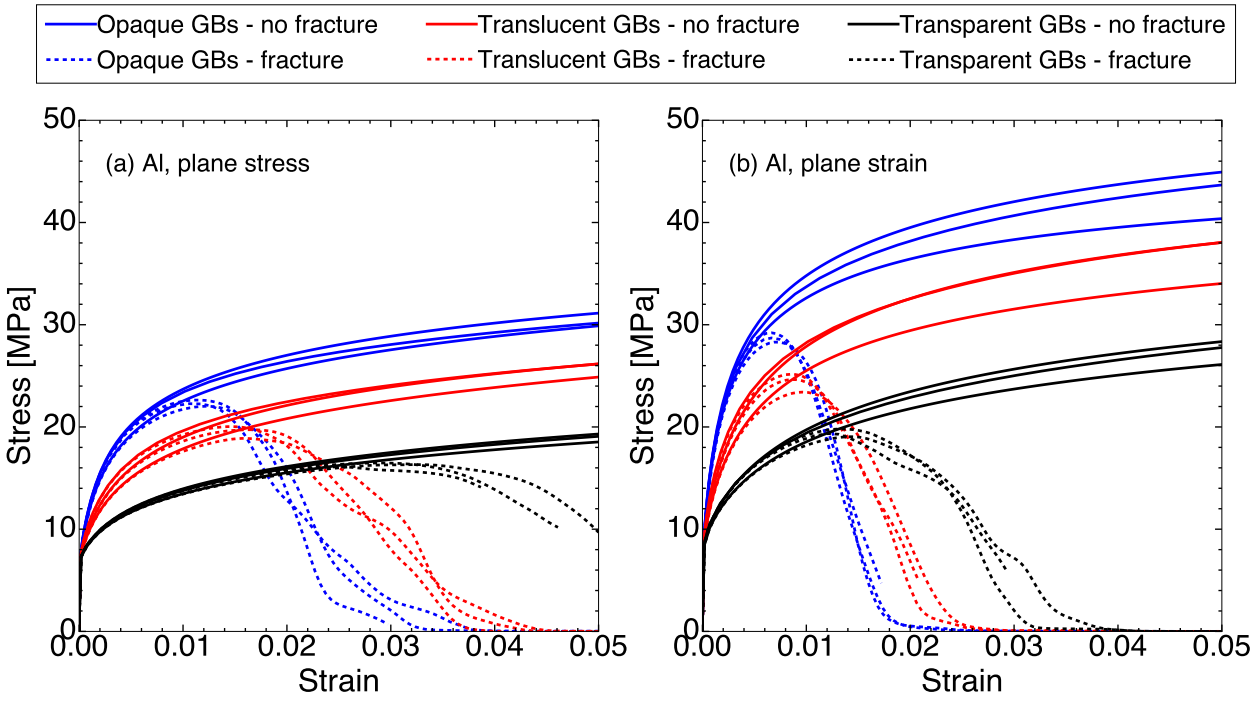

Figure 7.7: Engineering stress-strain curves of the Al (FCC) foils as a function of grain boundary type under (a) plane stress and (b) plane strain loading conditions. The solid lines correspond to the mechanical behavior without fracture, and the dashed lines correspond to simulations that include fracture at the GBs.

As observed in Chapter 6, the simulations with opaque GBs present the strongest tensile response, followed by those with translucent GBs, and finally by the simulations with fully transparent GBs. The simulations under plane strain generally present higher stresses than those under plane stress as a result of the restriction in the out-of-plane deformation, which leads to higher triaxiality. The simulations under plane stress present lower differences in the stress-strain curves between them for any GB character as compared with those carried out under plane strain (of the order of 5 MPa). These differences can also be attributed to the triaxiality.

The tensile stress-strain curves of the foils, including intergranular fracture, are super-

posed to those without cohesive surfaces until the onset of damage. While continuous strain hardening is observed in the foils without damage, the nucleation and growth of intergranular cracks lead to a maximum in the stress-strain curves, followed by a progressive reduction in the load-carrying capacity of the foil until complete fracture. The nucleation and progress of damage depended on the stress state (either plane stress or plane strain) and on the GB character. Fracture occurs sooner and progresses more rapidly under plane strain than under plane stress because of the higher stresses that facilitate the early fracture of the GBs. Moreover, damage initiation occurs sooner in the simulations with fully opaque GBs, followed by translucent GBs and fully transparent GBs simulations. This sequence is also repeated for the strain at the maximum stress as well as for the strain to failure.

The contour plots of the Von Mises stress (in MPa) and of the total dislocation density (in m^{-2}) are plotted in Fig. 7.8 for Al foil 1 under plane stress without fracture at ε = 2%. The results with fully opaque GBs are presented in the first row, with translucent GBs with slip transfer when $m' > 0.8$ in the second row, and with fully transparent GBs in the third row. Stress concentrations are found at the GBs along the center of the foil when all GBs are opaque, and they are associated with dislocation pile-up, as observed in the corresponding dislocation density contour plot. The stress concentrations gradually decrease for the translucent GBs, in which those GBs suitably oriented for slip transfer do not lead to stress concentrations, and the dislocation densities vary accordingly. Finally, high stress concentrations and dislocation pile-ups are not found in the case of fully transparent GBs. Stresses and dislocation densities are more homogeneous in this case, and moderate stress concentrations are found in smaller grains.

The effect of including intergranular fracture via cohesive surfaces in Al is plotted in Fig. 7.9 for foil 1 under plane stress at ε = 2%. The foils where intergranular fracture is not included are displayed on the left column, and the foils that incorporate intergranular fracture are displayed on the right column. As observed in the tensile curves for plane stress condition (Fig. 7.7 (a)), at ε = 2%, the foils with fully opaque GBs with intergranular fracture present a significant drop in the strength. As shown in the contour plots in the first row of Fig. 7.9, multiple cracks can already be observed at this strain, most of them in highly stressed GBs. The decrease in stiffness for the foils with translucent GBs at 2% deformation is not that dramatic, but there are some cracks with observable separation, also located at GBs with large local stresses. In the case of the foils with fully transparent GBs, the tensile test presents a negligible drop in the mechanical properties, and in fact, no evident cracks can be observed in the foil contour plots at this stage.

The final crack paths in the Al foil 1 are depicted in Fig. 7.10 as a function of GB character and loading conditions (plane stress or plane strain). The region most affected by fracture in the foils under plane stress is the left region, and fracture occurs in this region regardless of GB character. The foils with fully opaque and fully transparent GBs present almost the same crack path but not exactly the same. However, the foil with translucent GBs presents another crack at the middle-right region of the foil that does not appear in the other two cases. Regarding plane strain, the crack paths are very different for the three GB characters. Two main cracks appear at the two left and right ends of the foil in the foil with opaque

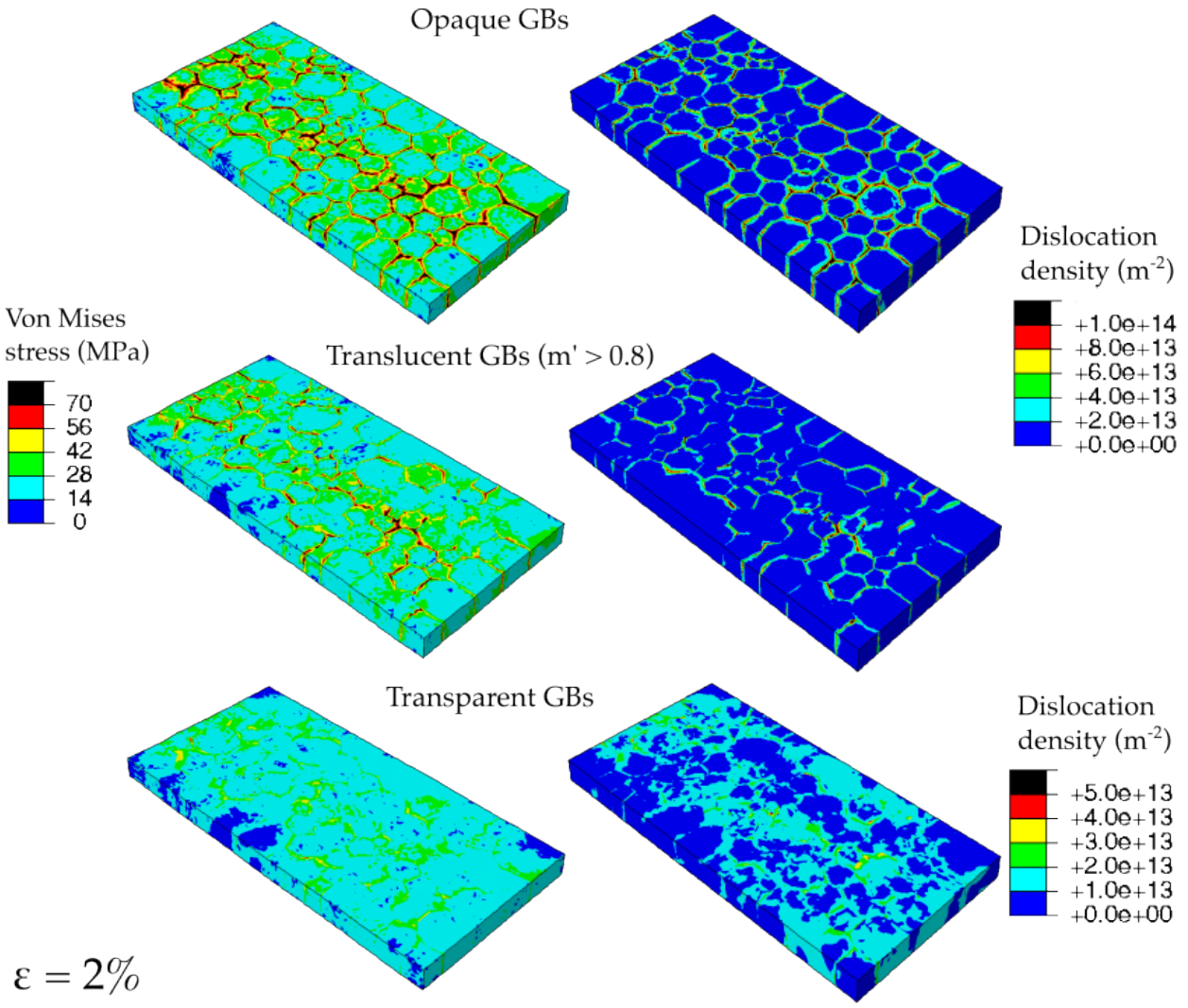

Figure 7.8: Contour plot of the Von Mises stress in MPa (left column) and of total dislocation density in m^{-2} (right column) at ε = 2% as a function of GB character in Al foil 1 under plane stress without fracture. The contour plots with fully opaque GBs are represented on the first row, with translucent GBs where slip transfer is allowed for $m' > 0.8$ on the second row and with transparent GBs on the third row. Note that a different scale is employed for the dislocation density for the foils with opaque and translucent GBs than that used for fully transparent GBs.

GBs, while the final crack appears at the right end (indicated with arrows in Fig. 7.10) with the translucent GBs, but the associated crack opening is very limited. Finally, the simulation with transparent GBs presents a complete separation from a catastrophic crack right in the middle of the foil. It should be noticed that many other GBs were damaged before the final fracture, but their fracture is not that evident in the contour plots in each foil. The final cracks of the other two Al foils also presented different paths depending on the GB character and loading conditions, but they are not provided for the sake of brevity.

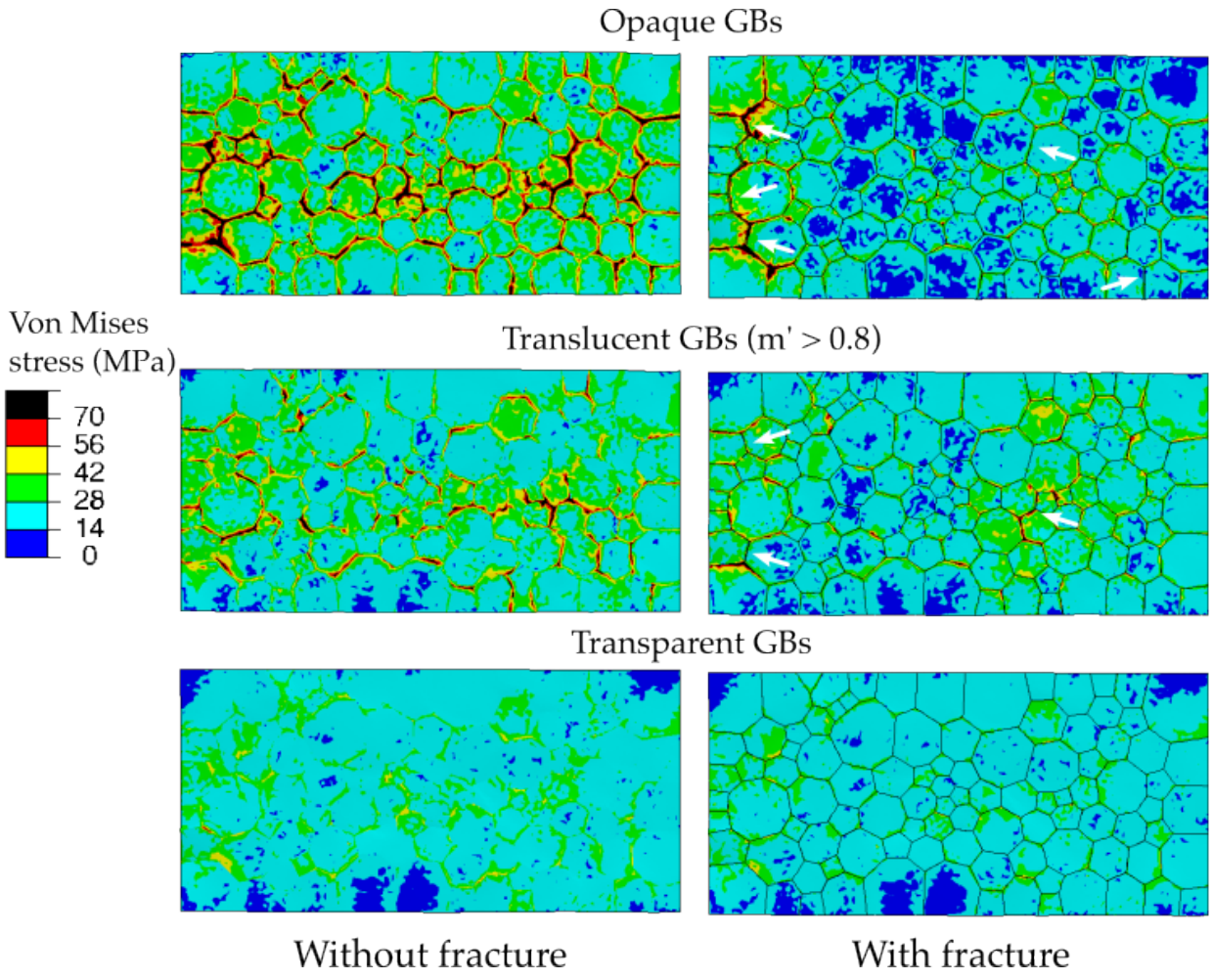

Figure 7.9: Contour plots of the Von Mises stress in MPa at ε = 2% without including fracture (left) and including intergranular fracture (right) as a function of GB character in Al foil 1 under plane stress. The contour plots with fully opaque GBs are represented on the first row, with translucent GBs where slip transfer is allowed for $m' > 0.8$ on the second row and with transparent GBs on the third row. Cracks are indicated by white arrows.

The effect of the different GB features –presented in Section 7.4– on the strain for damage initiation ε^0_{dmg} in the GBs was analyzed. To this end, the strain at which the first damage appeared in each GB was recorded and stored together with the GB features: α_x, $\mathrm{L_{GB}}$, Θ, $\overline{\mathrm{SA}}$, and $\mathrm{n_{Trs}}$. This database for the three Al thin foils is composed of 4760 damaged GBs, 2380 under plane stress, and 2380 under plane strain. The Pearson correlation coefficient matrix is plotted for ε^0_{dmg} and the different GB features in Fig. 7.11 for plane stress (a) and plane strain (b). The value of the Pearson correlation coefficient r is indicated at the center of each cell and also used as a heat map variable, ranging from -1 (pink) to +1 (orange), as indicated by the color bar on the right.

The Pearson coefficients r for the length of the GB $\mathrm{L_{GB}}$, the misorientation angle Θ, and the mean slip activation factor $\overline{\mathrm{SA}}$ are close to zero, indicating that there is no correlation

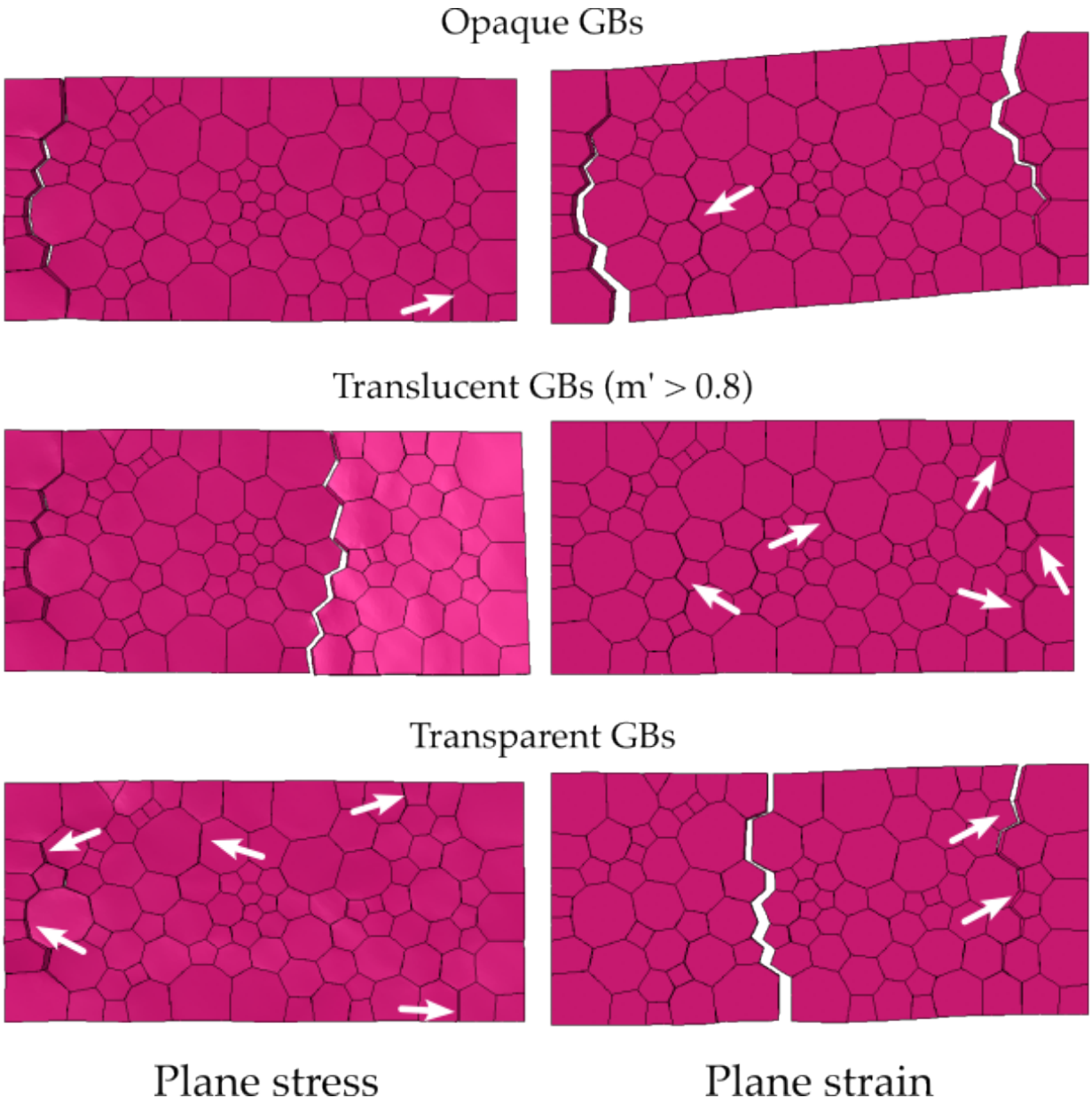

Figure 7.10: Crack path at the end of the simulations of Al foil 1 under plane stress (left column) and plane strain (right column) with fully opaque GBs (first row), translucent GBs where slip transfer is allowed for $m' > 0.8$ (second row), and transparent GBs (third row). The white arrows indicate the location of several intergranular cracks that are not evident in the figure.

between these variables and damage initiation. However, the angle between the GB and the loading axis α_x presents a moderate negative correlation with ε^0_{dmg} for both plane stress and plane strain. This indicates that the strain for damage initiation ε^0_{dmg} decreases when the angle α_x increases. In other words, those GBs perpendicular to the loading axis ($\alpha_x \approx 90°$) are prone to show damage nucleation at lower strains. The number of transparent slip systems $\mathrm{n_{Trs}}$ presents a moderate positive correlation with ε^0_{dmg}, and ε^0_{dmg} increases with

n_{Trs}. Hence, slip transfer delays the nucleation of damage in GBs, and conversely, those GBs with less transparent slip systems (or even opaque GBs with $n_{Trs} = 0$) will present premature damage initiation. The r values for α_x and n_{Trs} are of the same order for plane stress and plane stress. However, the strength of the correlation between n_{Trs} and ε^0_{dmg} is slightly higher than that of α_x for plane stress. This behavior could be explained by the fact that the GBs can couple the deformation with out-of-plane displacements under plane stress, and thus, the geometrical effect, governed by α_x, is not as important as the effect of GB character. Conversely, α_x presents the same correlation as n_{Trs} under plane strain, probably because the constraint of the out-of-plane motion enhances the effect of the geometry.

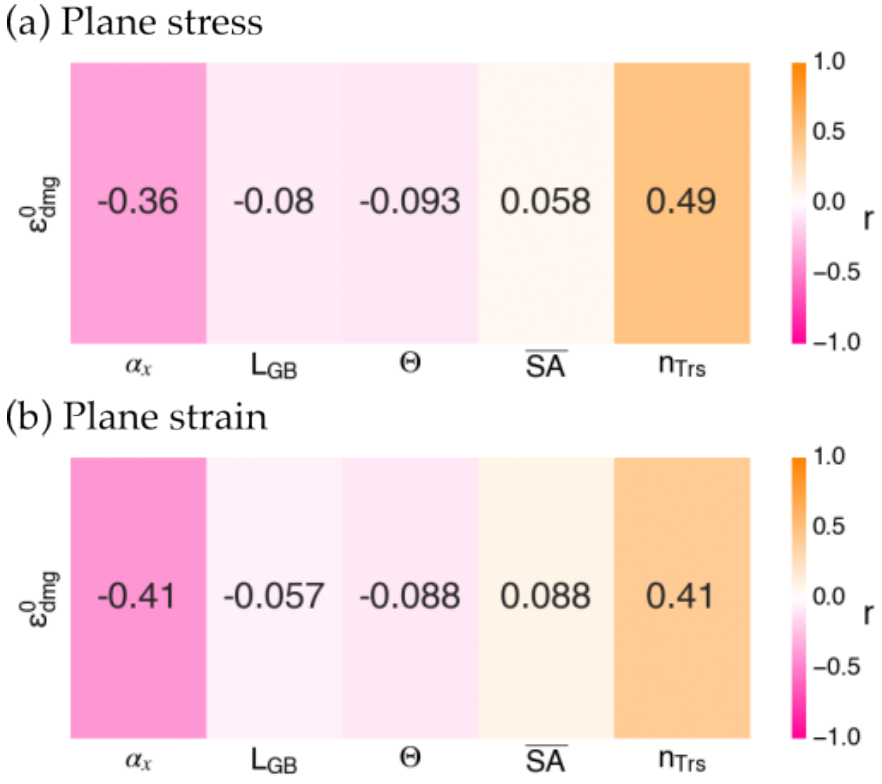

Figure 7.11: Pearson correlation matrix for GB fracture in the Al foils. (a) Plane stress, (b) plane strain.

In summary, the two GB features that have an effect on damage nucleation in FCC Al foils are the angle between the GB and the loading axis α_x and the number of transparent slip systems in a GB, n_{Trs}. The GBs that may lead to premature damage nucleation are those nearly perpendicular to the loading axis and those opaque or nearly opaque to dislocations. On the contrary, the GB length L_{GB}, the misorientation angle Θ, and the slip activation factor $\overline{SA}$ are not correlated with the onset of damage at GBs.

7.5.2 Intergranular fracture of Mg foils in tension (random texture)

The tensile stress-strain curves of the two Mg foils with random crystal orientations (foils 1 and 3 in Fig. 7.4), with and without fracture, are plotted in Fig. 7.12 as a function of GB character under plane stress (a), and plane strain (b) loading conditions. The simulations without fracture are represented with solid lines, and the simulations that include fracture through cohesive surfaces are plotted with dashed lines.

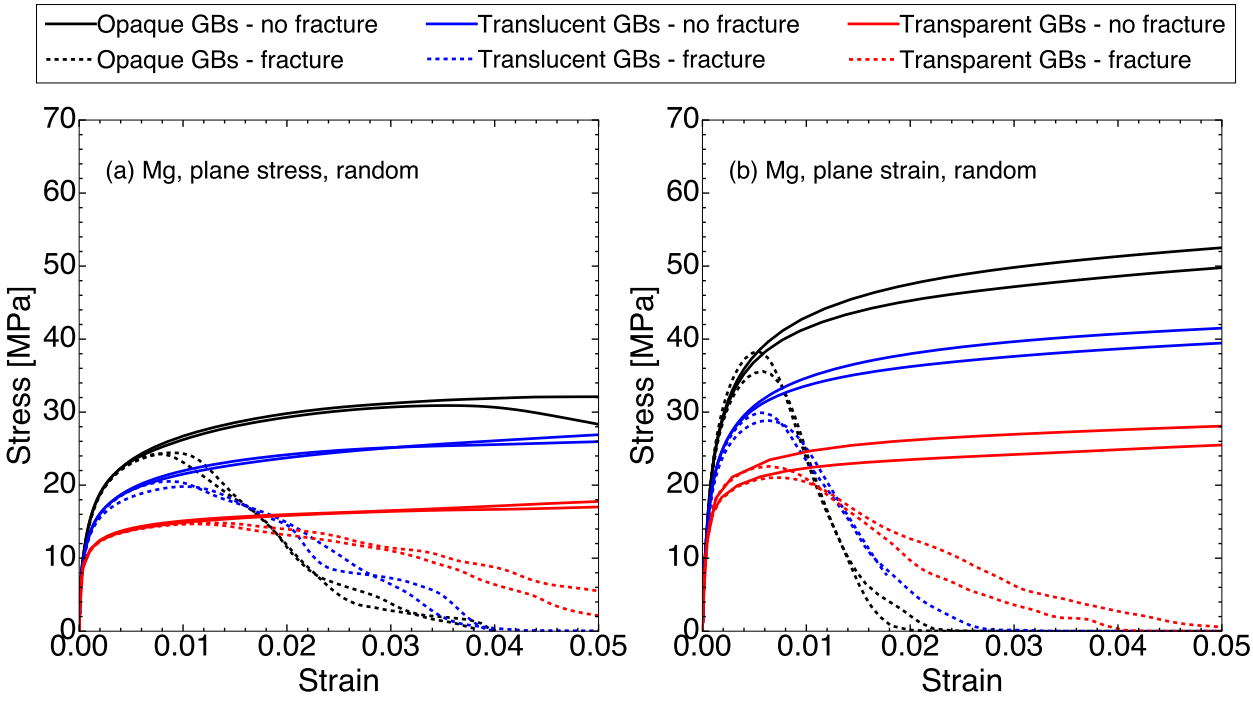

Figure 7.12: Engineering stress-strain curves of the Mg thin foils with random orientations (foils 1 and 3) as a function of GB type under (a) plane stress and (b) plane strain loading conditions. The solid lines correspond to the mechanical response of the foils without fracture, while the dashed lines include fracture at GBs.

As in the case of FCC Al, the HCP Mg foils with fully opaque GBs present the strongest tensile response, followed by translucent GBs and transparent GBs. Similarly, the stress-strain curves obtained under plane strain are displaced towards higher stresses because of the larger triaxiality. The curves of the two foils do not present great differences between them, but this difference increases under plane strain loading conditions. When GBs are assumed to be translucent or fully transparent in HCP metals, stress concentrations mainly arise because of the deformation incompatibility between grains with different crystal orientations. This behavior applies to both loading conditions, plane stress (Fig. 7.12 (a)) and plane strain (Fig. 7.12 (b)).

Regarding fracture, damage is nucleated early and evolves faster for plane strain than for plane stress, as in the case of the Al foils, because of the enhanced triaxiality. In addition, the GB character (opaque, translucent, or transparent) has an effect on damage nucleation and propagation, but it is clearly smaller than in the case of FCC Al. For instance, the strain

at the maximum stress is very similar for the three types of GBs in both plane stress and plane strain, although the maximum stress is significantly higher for the opaque GBs. This may suggest that HCP materials are not as sensitive to the GB character as FCC materials.

The contour plots of the Von Mises stress (in MPa) and of the total dislocation density (in m^{-2}) are plotted in Fig. 7.13 for Mg foil 1 under plane stress without fracture at 2% deformation. The results with fully opaque GBs are presented in the first row, with translucent GBs with slip transfer when $m' > 0.8$ in the second row, and with fully transparent GBs in the third row. The contour plots of the Von Mises stress in the foil with opaque shows that stress concentrations at the GBs are localized in a limited number of GBs while they were more homogeneously distributed in the FCC Al foil. Similar differences between HCP Mg and FCC Al can be found in the foils with translucent and transparent GBs, although the number of GBs with stress concentrations decreases in both cases as slip transfer is allowed through the GB. These results indicate that the deformation incompatibility between adjacent grains in HCP Mg leads to the development of stress concentrations at GBs, even in the case of the foil with fully transparent GBs. Regarding dislocation density, dislocation pile-ups appear at GBs when they are assumed as fully opaque, but the distribution of GBs with large dislocation densities is more inhomogeneous than in the case of the FCC Al foil, and the dislocation density in some GBs in HCP Mg foils is only slightly higher than that in the bulk. When slip transfer is allowed, more GBs become transparent to dislocations, and the total dislocation density decreases. Finally, the dislocation density is approximately one order of magnitude smaller for the foil with fully transparent GBs, but there are still some regions with high dislocation density that are associated with stress concentrations at GBs due to the incompatibility of deformation between grains. Hence, stress concentrations at GBs in HCP Mg foils are determined by the GB character (either opaque, translucent, or transparent) and by the orientation of the grains around the GB that may lead to the development of stress concentrations to accommodate the incompatibility of plastic deformation between grains.

The effect of including intergranular fracture via cohesive surfaces in Mg is plotted in Fig. 7.14 for foil 1 (with random crystal orientations) under plane stress at ε = 2%. The foils without intergranular fracture are displayed on the left column, and the foils that incorporate intergranular fracture are displayed on the right column. As observed in the tensile stress-strain curves under plane stress (Fig. 7.12 (a)), at ε = 2%, all the three foils (fully opaque, translucent, and fully transparent GBs) present a significant drop in the strength when interface fracture is included. Multiple cracks are observed for the foil with opaque GBs at this strain (Fig. 7.14), most of them located within the most stressed region. This is also the case for translucent GBs, where the number of cracks is smaller, but they are also located in regions where the stresses are higher. Finally, the foil with fully transparent GBs just presents a few cracks because, as shown in the tensile test (Fig. 7.12 (a)), the fracture is delayed to higher strains.

The final crack paths in the Mg foil 1 with random texture are depicted in Fig. 7.15 as a function of GB character and loading conditions (plane stress or plane strain). Cracking occurs in different locations depending on the GB character and the loading conditions, as in the Al foil. Fracture generally occurs at the left region of the foils under plane stress,

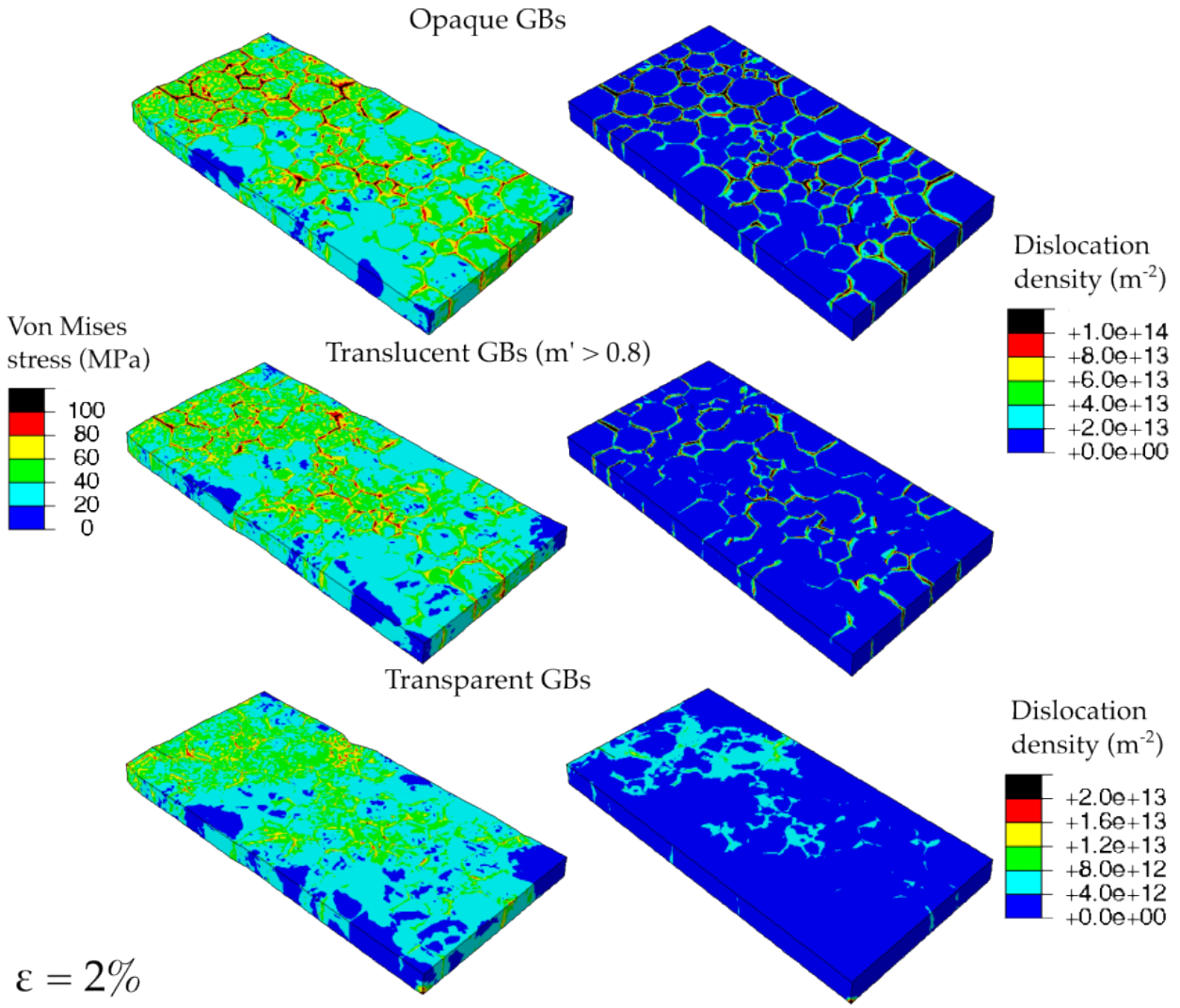

Figure 7.13: Contour plot of the Von Mises stress in MPa (left column) and of total dislocation density in m^{-2} (right column) at ε = 2% as a function of GB character in Mg foil 1 (random texture) under plane stress without fracture. The contour plots with fully opaque GBs are represented on the first row, with translucent GBs where slip transfer is allowed for $m' > 0.8$ on the second row and with transparent GBs on the third row. Note that a different scale is used for the dislocation density of the foils with opaque and translucent GBs and for the fully transparent GBs.

but the crack path differs depending on the GB character. However, there is a significant number of damaged GBs that are common to the three GB characters. Regarding the simulations under plane strain, the foils with opaque and translucent GBs present a very similar crack path along the central section of the foil. However, the foil with transparent GBs presents a different crack path, more similar to the ones found under plane stress.

The effect of the different GB features on the strain for damage initiation ε^0_{dmg} was also analyzed in the HCP Mg foils with random texture following the same strategy used in

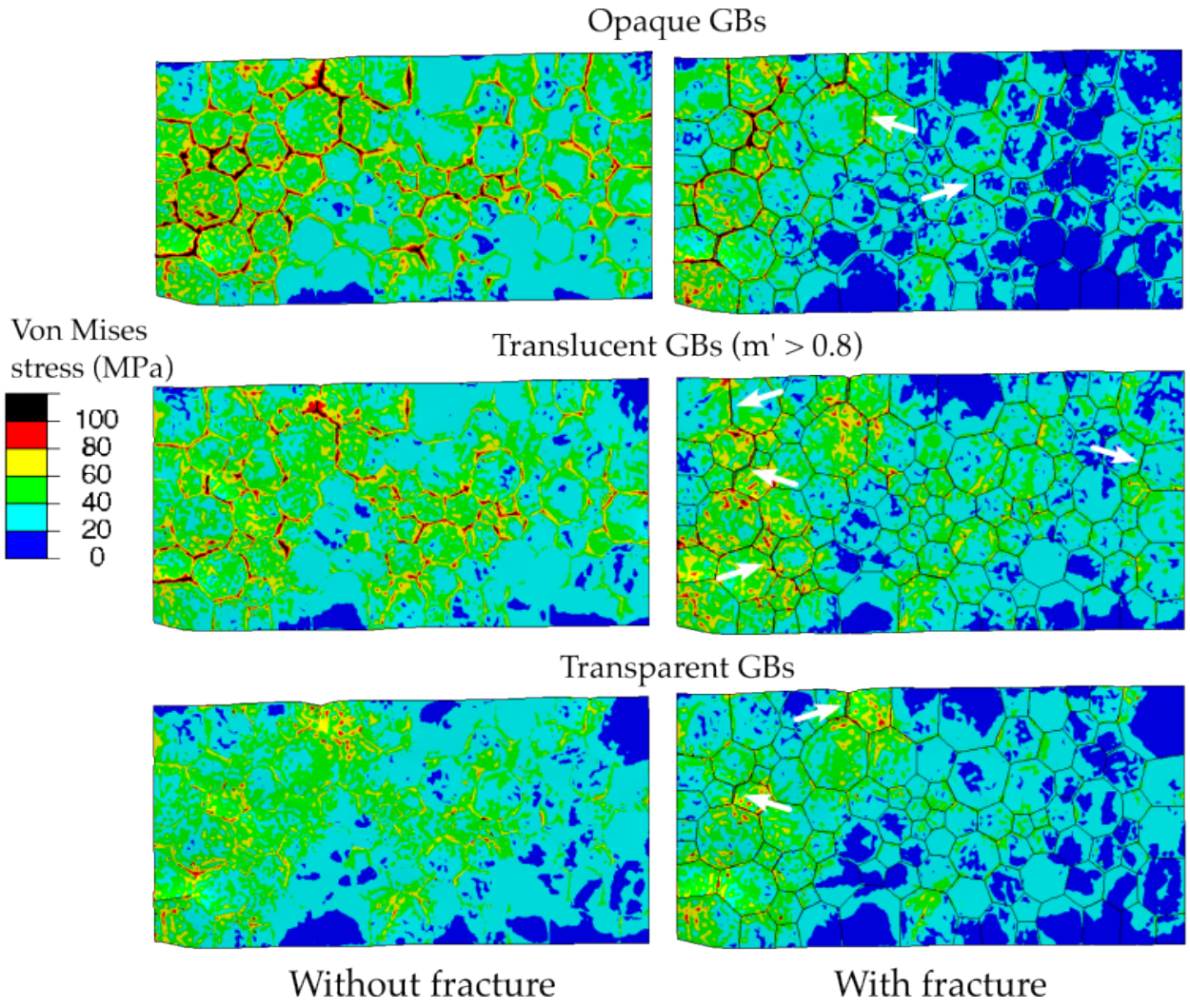

Figure 7.14: Contour plots of the Von Mises stress in MPa at ε = 2% without intergranular fracture (left) and with intergranular fracture (right) as a function of GB character in the Mg foil 1 under plane stress. The contour plots with fully opaque GBs are represented on the first row, with translucent GBs where slip transfer is allowed for $m' > 0.8$ on the second row and with transparent GBs on the third row. The white arrows indicate the location of intergranular cracks.

the Al foils. Besides the GB features used for FCC Al (α_x, $\mathrm{L_{GB}}$, Θ, and $\mathrm{n_{Trs}}$), the mean slip activation factors for basal, prismatic, and pyramidal slip, $\overline{\mathrm{SA}}_{\mathrm{b}}$, $\overline{\mathrm{SA}}_{\mathrm{p}}$, and $\overline{\mathrm{SA}}_{\mathrm{py}}$, respectively, were included in the analysis. The dataset for Mg with random texture is composed of 3141 fractured GBs for the two thin foils, classified as 1562 under plane stress and 1579 under plane strain. The Pearson correlation matrices for plane stress and plane strain are presented in Fig. 7.16 and visually display the influence of the GB features on ε^0_{dmg}.

The damage analysis for the simulations under plane stress indicated that the angle α_x between the GB and the loading axis presents a moderate negative correlation with the strain for damage initiation ε^0_{dmg}. This means that GBs that are perpendicular to the loading axis

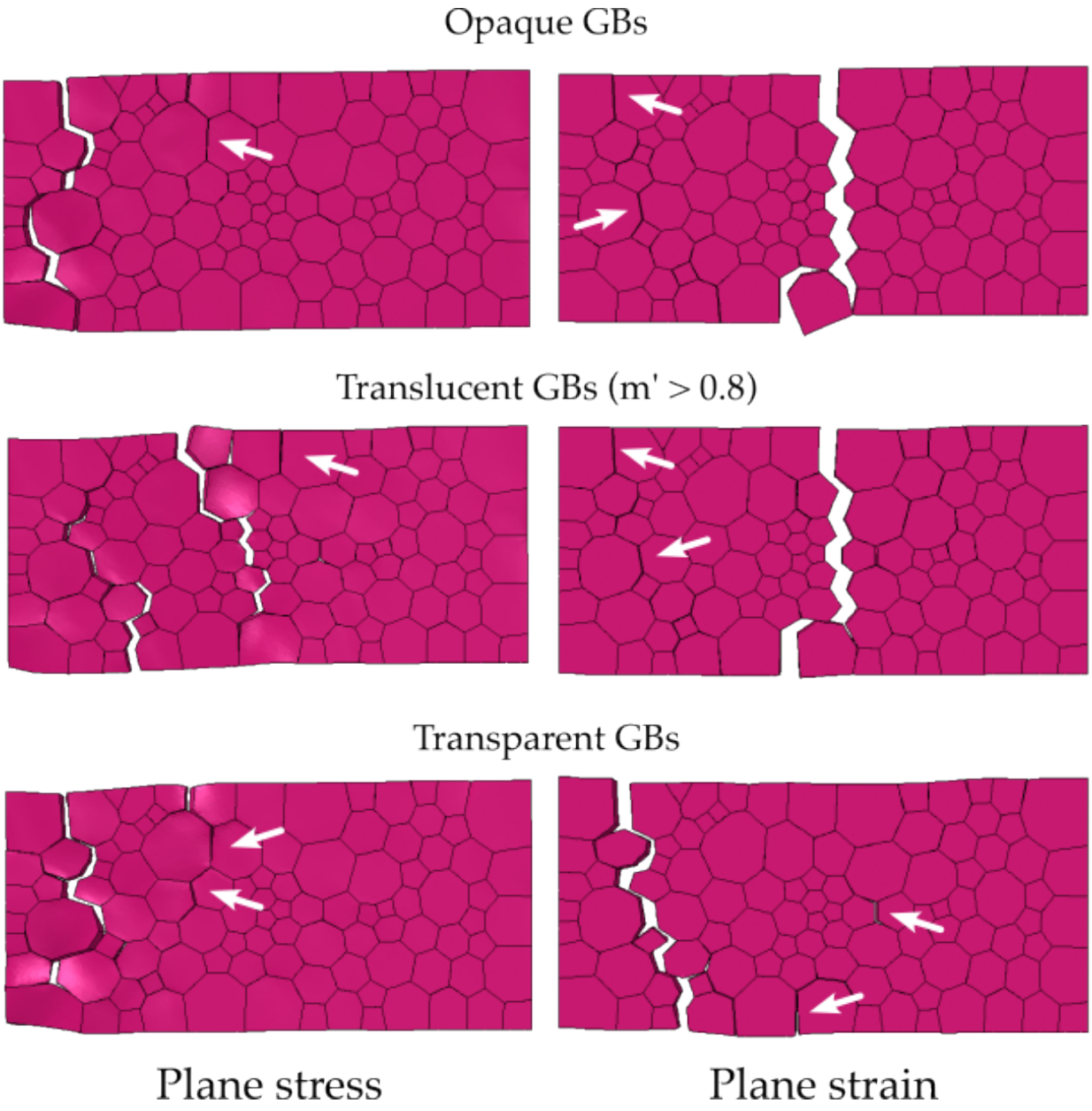

Figure 7.15: Crack path at the end of the simulations of Mg foil 1 with random crystal orientations under plane stress (left column) and plane strain (right column) with fully opaque GBs (first row), translucent GBs where slip transfer is allowed for $m' > 0.8$ (second row), and transparent GBs (third row).

are prone to damage nucleation at lower strains. $\mathrm{L_{GB}}$, Θ, and $\overline{\mathrm{SA}}_{\mathrm{py}}$ show a near-zero correlation on ε^0_{dmg}, and thus, they do not influence damage nucleation. However, a noticeable linear correlation between $\overline{\mathrm{SA}}_{\mathrm{b}}$ with ε^0_{dmg}, comparable to that observed for α_x, is noticed in the HCP Mg foils. This result is different from the one reported in FCC Al foils, where the average slip activation factor showed negligible correlation with damage initiation. The Pearson correlation values of the basal and the prismatic slip activation factors have

Figure 7.16: Pearson correlation matrix for GB fracture in the Mg foils with random crystal orientations. (a) Plane stress, (b) plane strain.

opposite signs, with negative Pearson correlation for $\overline{\mathrm{SA}}_{\mathrm{b}}$ and positive for $\overline{\mathrm{SA}}_{\mathrm{p}}$. This is in agreement with the geometry of the hexagonal lattice because basal and prismatic planes are perpendicular, and when one is well-oriented for slip, the other is not. According to the Pearson correlation values, damage at GBs occurs earlier when the grains across a GB are well-oriented for basal slip, and thus $\overline{\mathrm{SA}}_{\mathrm{b}}$ is high. Taking into account that the CRSS for basal slip is very low, plastic deformation will be localized in the grains with high $\overline{\mathrm{SA}}_{\mathrm{b}}$ across the GB, and the accommodation of the large plastic deformation in these grains with other stiffer grains in the neighborhood may lead to the appearance of stress concentrations at the GBs and, eventually, to fracture. Finally, the number of transparent slip systems $\mathrm{n}_{\mathrm{Trs}}$ presents a weak positive correlation with ε^0_{dmg}, meaning that those GBs opaque to dislocations could be more likely to early damage nucleation. This correlation is significantly smaller than in Al and may suggest that GB character has a lower effect on damage initiation in HCP Mg than in FCC Al.

This analysis was also performed for the foils under plane strain, and the results are similar. A stronger (but moderate) correlation is observed for α_x, higher than in the case of plane stress. Apart from this, the effect of the slip activation factor $\overline{\mathrm{SA}}_{\mathrm{b}}$ decreases with respect to the plane stress conditions, and its Pearson correlation coefficient is now comparable to that of the number of transparent slip systems $\mathrm{n}_{\mathrm{Trs}}$. This means the texture and the effect of the GB character play minor roles in damage nucleation under plane strain because the higher stress levels favor the stronger effect of the angle between GB and the loading axis.

7.5.3 Intergranular fracture of Mg foils in tension (basal texture)

The tensile stress-strain curves of the two Mg foils with strong basal texture (foils 2 and 4 in Fig. 7.4), with and without fracture, are plotted in Fig. 7.17 as a function of GB character under plane stress (a), and plane strain (b) loading conditions. The simulations without fracture are represented with solid lines, while those with fracture through cohesive surfaces are plotted with dashed lines.

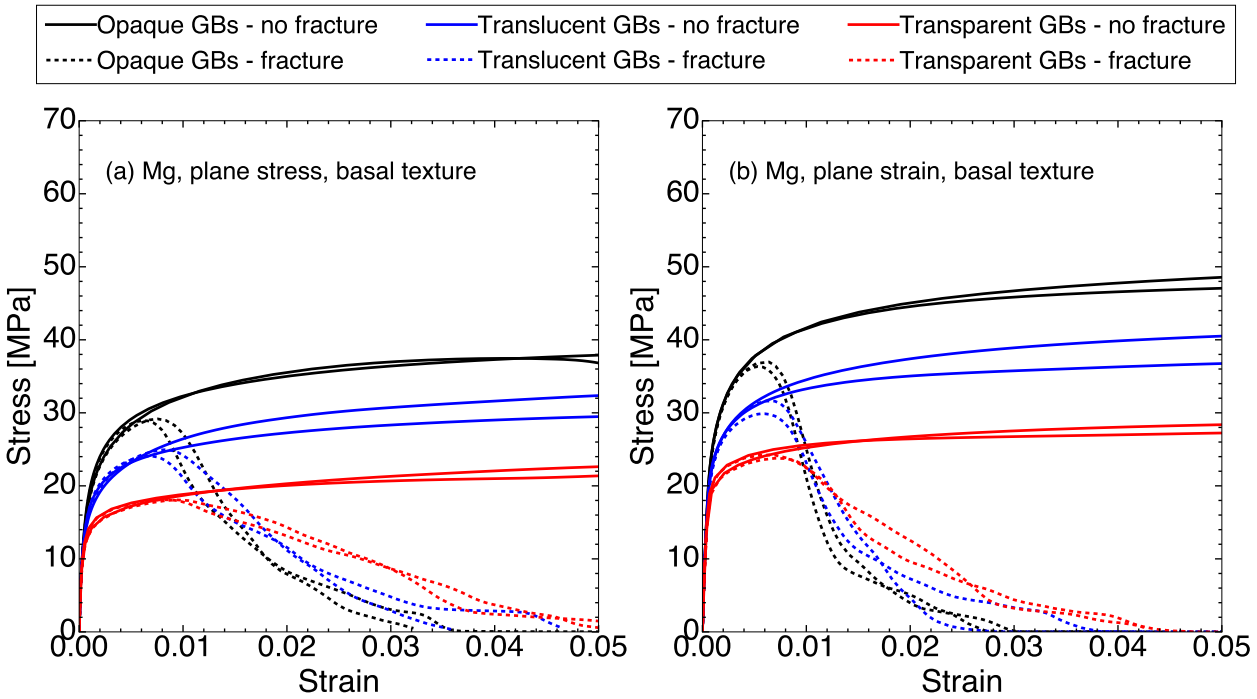

Figure 7.17: Engineering stress-strain curves of the Mg thin foils with basal texture (foils 2 and 4) as a function of GB type under (a) plane stress and (b) plane strain loading conditions. The solid lines correspond to the mechanical response of the foils without fracture, while the dashed lines include fracture at GBs.

The foils with fully opaque GBs present the strongest mechanical response, followed by translucent GBs and transparent GBs, as reported in the two previous cases (FCC Al and HCP Mg with random texture). Similarly, the stress-strain curves under plane strain are displaced towards higher stresses because of the triaxiality. The curves of the different foils do not present great differences in the case of strong basal texture, especially when GBs are fully opaque or fully transparent.

Regarding fracture, damage initiates early and grows at a faster rate for plane strain than for plane stress, as observed in the Mg foils without texture. The GB character (opaque, translucent, or transparent) does not seem to affect damage nucleation and propagation since the strain at the maximum stress and the damage propagation are very similar for the three types of GBs in both plane stress and plane strain. This reinforces the idea that HCP materials are not as sensitive to the GB character as FCC materials.

The contour plots of the Von Mises stress (in MPa) and of the total dislocation density (in

m^{-2}) are plotted in Fig. 7.18 for Mg foil 2 with basal texture under plane stress without fracture at 2% deformation. The results with fully opaque GBs are presented in the first row, with translucent GBs with slip transfer when $m' > 0.8$ in the second row, and with fully transparent GBs in the third row. As observed in the contour plots, stress concentrations are found at some GBs in the foils with opaque GBs but not in all of them. The stress concentrations decrease as the GBs become translucent and transparent, but they appear even in the latter due to the deformation incompatibility between adjacent grains. These stress concentrations appear at the regions where the crystal orientations between the adjacent grains are very different, like the left region of the foil (see Fig. 7.4 (b)). Conversely, when the grain orientations and the dominant deformation mechanisms are compatible, as in the central section of the foil, no large stress concentrations appear, regardless of the GB character.

The effect of intergranular fracture is depicted in the contour plots in Fig. 7.19 for foil 2 (with strong basal texture) under plane stress at ε = 2%. The foils without fracture are displayed on the left column, and the foils that incorporate intergranular fracture are displayed on the right column. As observed in the tensile stress-strain curves for plane stress (Fig. 7.17 (a)), at ε = 2%, all the three foils (fully opaque, translucent, and fully transparent GBs) present a significant drop in the strength. Multiple cracks are observed for the foil with opaque GBs at this strain (Fig. 7.19), and most of them are located on the left side of the foil, in which large stress concentrations at GBs can be found. This is also the case for translucent GBs, where the number of cracks is smaller, but they are also located in regions where the stresses are higher. Finally, the foil with fully transparent GBs just presents a few cracks because, as shown in the tensile test (Fig. 7.17 (a)), fracture is delayed to larger applied strains.

The final crack paths in Mg foil 2 with basal texture are depicted in Fig. 7.20 as a function of GB character and loading conditions (plane stress or plane strain). Cracking occurs in more similar locations depending on the GB character and the loading conditions in comparison to the Mg foil without texture (see Fig. 7.15). In this case, the fracture is localized on the left region of the foils regardless of the GB character and the loading conditions, but the crack path is different for plane stress and plane strain. Nevertheless, the GB character seems to have a smaller effect on the location of the final crack in comparison to that observed in the foil with random texture.

Due to the plastic anisotropy of HCP Mg, crystallographic texture may have an important effect on the tensile response of the foil. The tensile stress-strain curves of the Mg foils with random texture (foils 1 and 3) and with strong basal texture (foils 2 and 4) with and without intergranular fracture are presented in Fig. 7.21 (a) for fully opaque GBs and plane stress. The stress-strain curves with and without texture present a similar shape, but the foils with basal texture are displaced towards slightly higher stresses (about 5 MPa difference). The stiffer response of the foils with basal texture can be explained by the enhanced activation of prismatic slip, which requires higher CRSS and thus hardens the material. Conversely, when the crystal orientations are random, basal slip will be facilitated due to its small CRSS, which provides a softer response.

To illustrate this, the relative contributions of the different slip systems in the HCP lattice

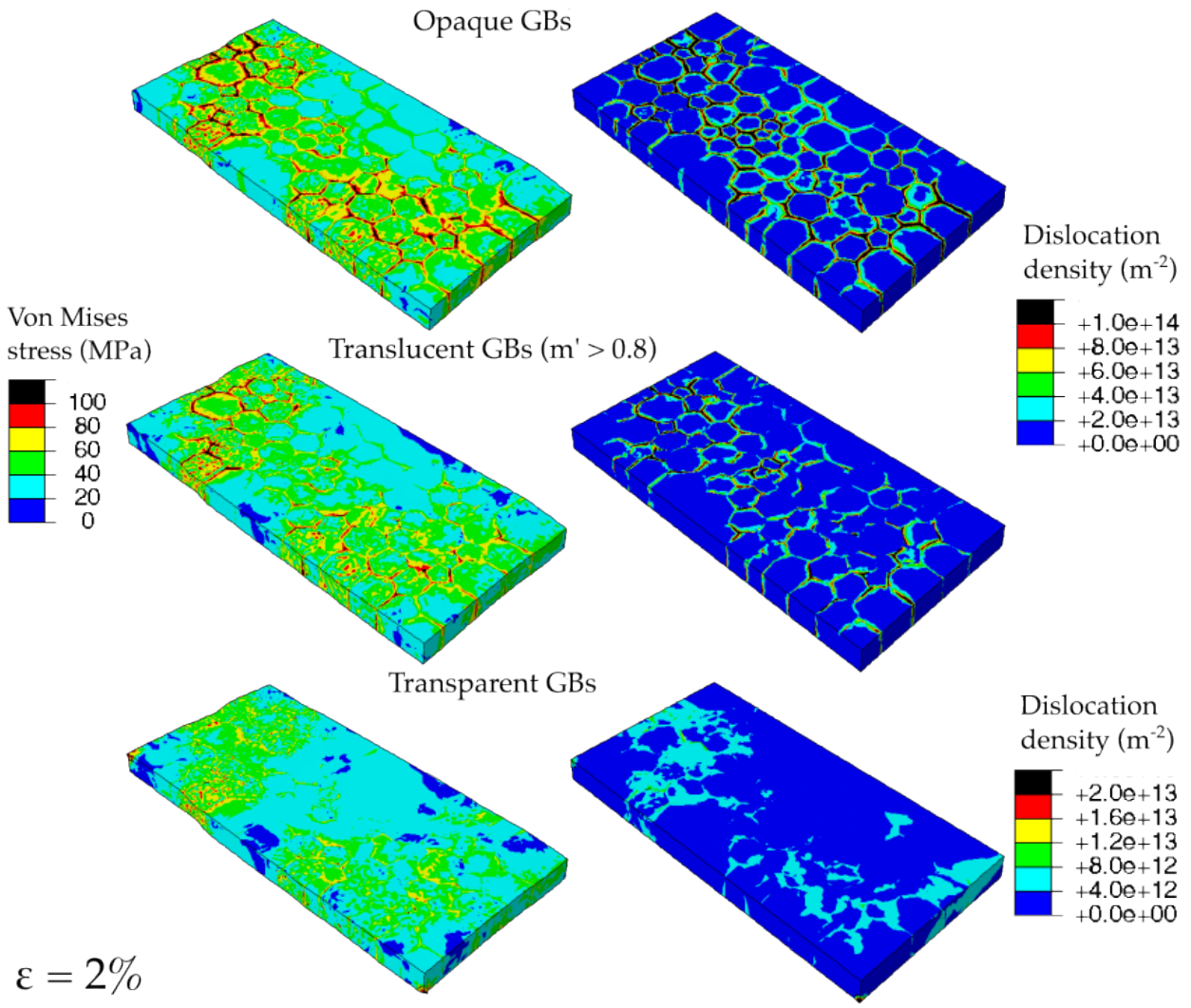

Figure 7.18: Contour plot of the Von Mises stress in MPa (left column) and of total dislocation density in m^{-2} (right column) at ε = 2% as a function of GB character in Mg foil 2 (strong basal texture) under plane stress without fracture. The contour plots with fully opaque GBs are represented on the first row, with translucent GBs where slip transfer is allowed for $m' > 0.8$ on the second row and with transparent GBs on the third row. Note that a different scale is employed for the dislocation density for the foils with opaque and translucent GBs and for those with fully transparent GBs.

to the accumulated plastic slip γ are plotted in Fig. 7.21 (b) for foils 1 (random orientations, solid lines) and 2 (basal texture, dashed lines) and plane stress. The strong effect of texture on the deformation mechanisms is shown in this figure. In general, basal slip dominates over the other slip systems at the early stages of deformation when the stresses are low. The contribution of prismatic slip increases with applied strain as the stresses are large enough to overcome its CRSS (refer to Table 6.5). The contribution of pyramidal slip is always very small. The main contribution to the plastic deformation under plane stress and random texture always comes from basal slip in the whole strain range (about 65%),

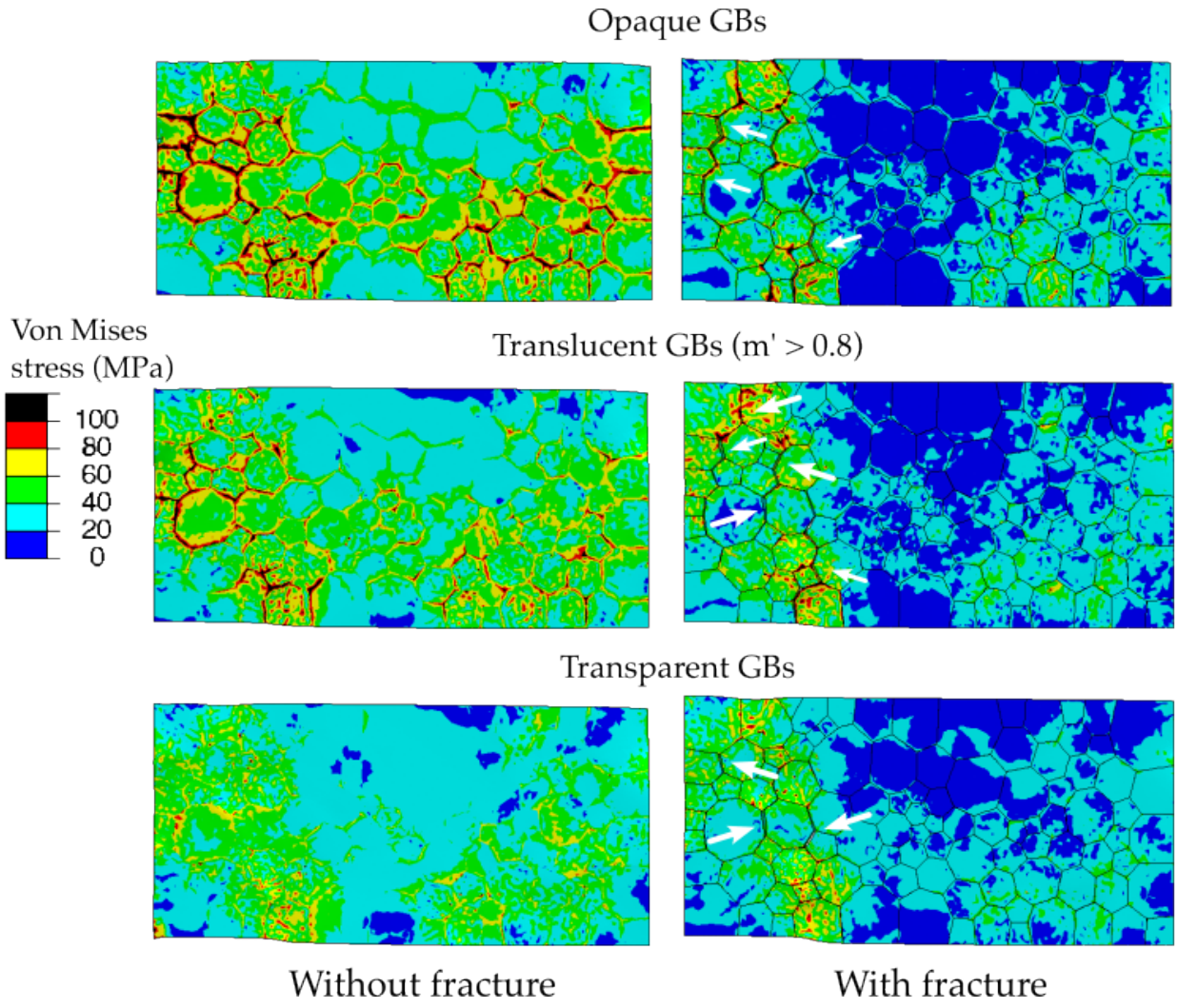

Figure 7.19: Contour plots of the Von Mises stress in MPa at ε = 2% without including fracture (left) and including intergranular fracture (right) as a function of GB character in Mg foil 2 under plane stress. The contour plots with fully opaque GBs are represented on the first row, with translucent GBs where slip transfer is allowed for $m' > 0.8$ on the second row and with transparent GBs on the third row. Intergranular cracks are indicated with white arrows.

followed by prismatic (about 30%) and pyramidal slip (less than 5%). However, basal slip and prismatic slip contribute equally to plastic slip (about 50% each) in the foil with strong basal texture, while the contribution of pyramidal slip is negligible. It should be noticed that the basal texture promotes the activation of prismatic slip instead of basal slip because the basal planes are nearly parallel to the loading axis. Thus, the activation of prismatic slip, which requires higher CRSS, induces a strengthening effect on the tensile response of the foils with a strong basal texture. However, the CRSS for basal slip in Mg is very small -as compared to those of prismatic and pyramidal – so basal slip is always active. These two factors lead to a competitive process between basal and prismatic slip activation, whose contributions would probably be balanced above 5% strain.

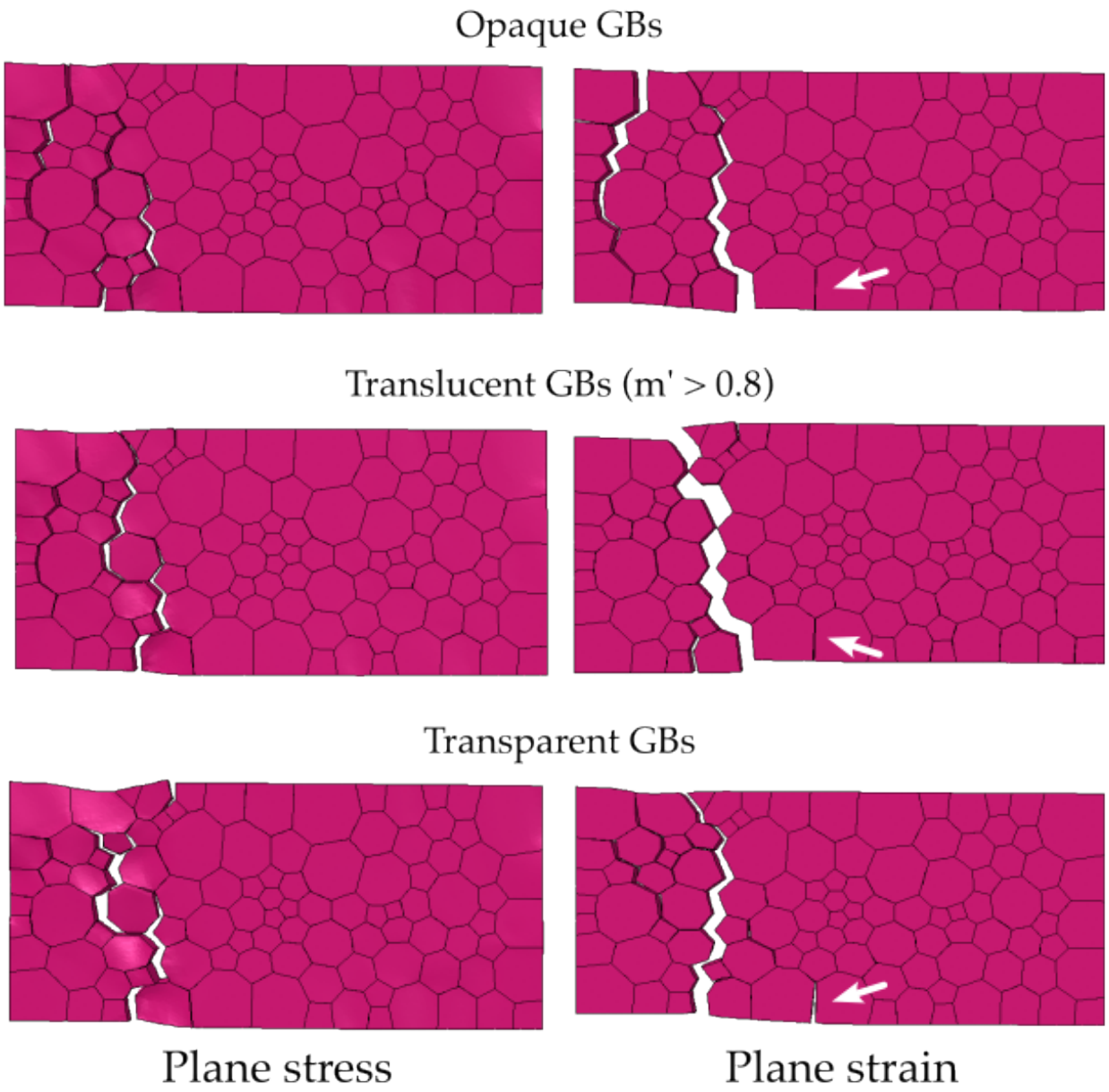

Figure 7.20: Crack path at the end of the simulations of Mg foil 1 with basal texture under plane stress (left column) and plane strain (right column) with fully opaque GBs (first row), translucent GBs where slip transfer is allowed for $m' > 0.8$ (second row), and transparent GBs (third row).

The effect of texture on the strength of the foils is different under plane strain (Fig. 7.22 (a)), and the foils with random texture are slightly stronger than those with random texture. Plane strain leads to a greater increase in the strength of the foils with random texture than in those with basal texture because the out-of-plane displacements necessary to accommodate the deformation incompatibility between adjacent grains with very different crystal orientations are hindered. On the contrary, out-of-plane displacements are less crit-

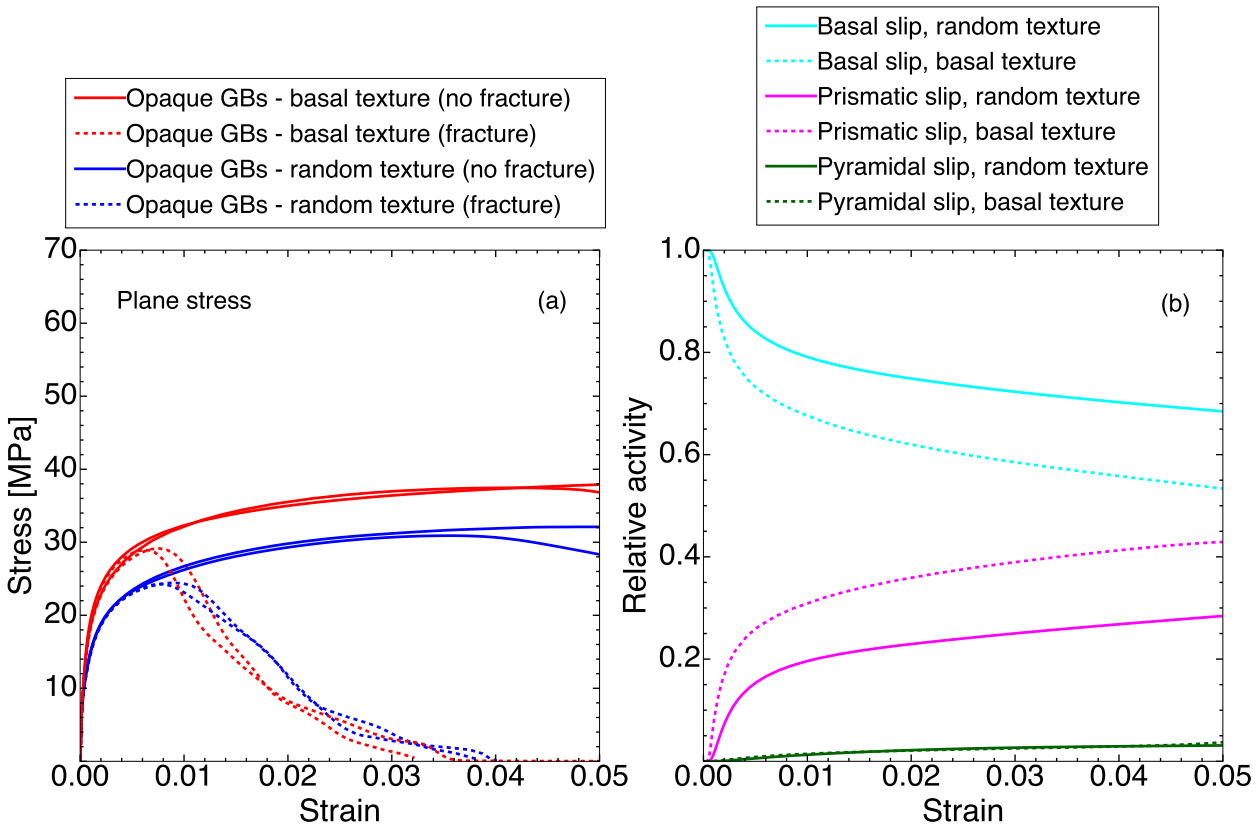

Figure 7.21: (a) Engineering stress-strain curves of Mg thin foils with random crystal orientations (foils 1 and 3, in blue) and with strong basal texture (foils 2 and 4, in red) with opaque GBs under plane stress. The solid lines correspond to the foils without fracture, and the dashed lines correspond to the foils with fracture. (b) Relative contribution of the basal, prismatic, and pyramidal slip systems to the accumulated plastic slip γ as a function of the crystallographic texture in Mg thin foils 1 (random orientations, solid lines) and 2 (basal texture, dashed lines) with fully opaque GBs under plane stress conditions.

ical in the foils with basal texture because of the orientation similarity between neighbor grains. Hence, the difference in the tensile response under plane stress and plane strain between random and basal texture could be attributed to the conjoint effect of the out-of-plane constraint, which increases triaxiality, and the crystallographic texture. Regarding intergranular fracture, the presence of crystallographic texture does not seem to play any role since the tensile responses for foils 1 and 2 are very similar in terms of both the strain for damage nucleation and the damage propagation rate.

Regarding slip system activity, the plane strain simulations present a similar behavior to that observed under plane stress but modified by the higher stresses applied on the foils (Fig. 7.22 (b)). They promote a significant contribution of prismatic slip from the early stages of deformation. Moreover, the contribution of pyramidal slip is also greater than for plane stress, but it is still negligible as compared to basal or prismatic. Basal slip is dominant for the simulations with random texture (about 60%), followed by prismatic

with about 30% contribution to γ. However, prismatic slip clearly dominates over basal slip –even below 1% deformation– in the foil with strong basal texture. The effect of crystallography and texture is once again enhanced by the plane strain constraint to the foil plane, which drastically increases the stress level and the activation of prismatic slip. On one hand, the basal texture promotes the dominant activation of prismatic slip with higher CRSS, which provides a strengthening effect in the tensile response. On the other hand, in the foils with random orientations, the main contribution to the accumulated plastic slip comes from the softer basal slip due to its ease of activation. Nevertheless, the out-of-plane constraint, together with the orientation differences between adjacent grains, increases the stress triaxiality, thus providing a harder tensile response. Summing all these effects, the tensile curves of the foils with and without texture look very similar despite the fact that the plastic deformation mechanisms are significantly different.

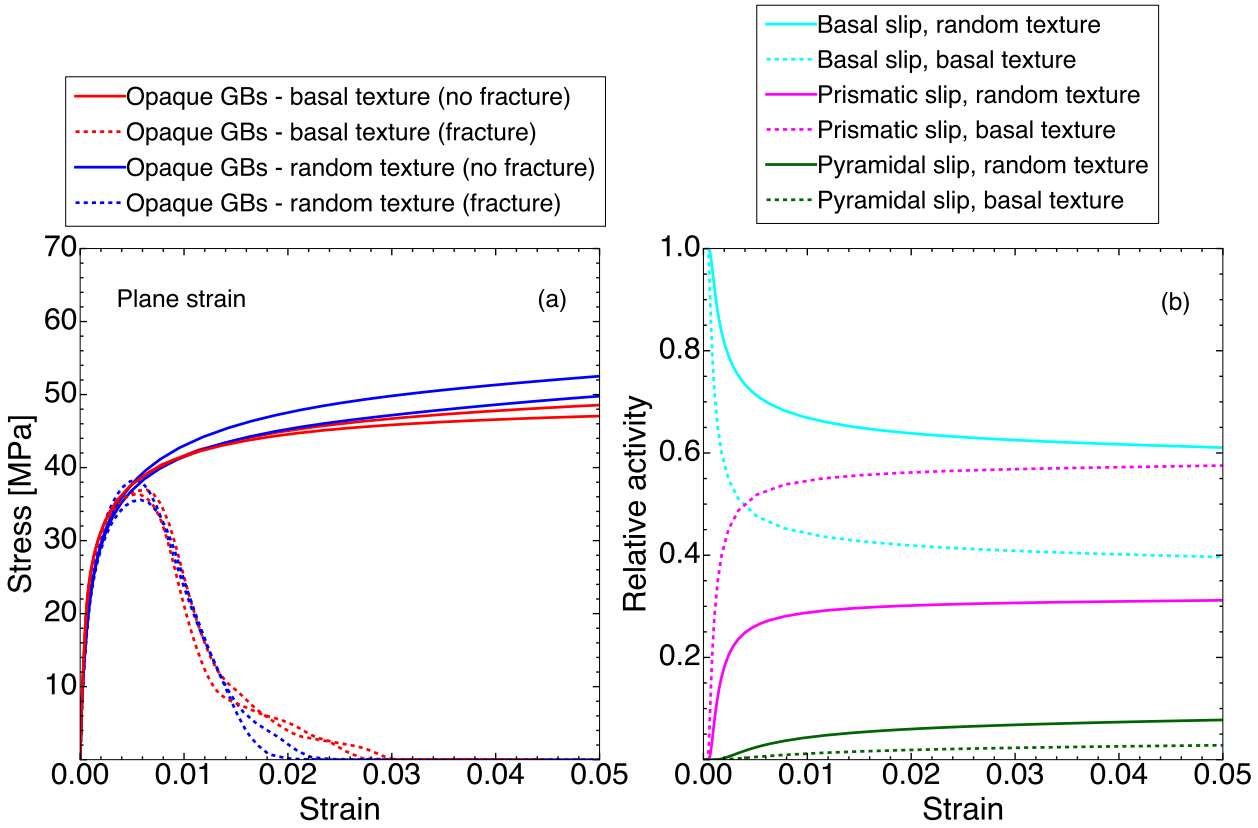

Figure 7.22: (a) Engineering stress-strain curves of Mg thin foils with random crystal orientations (foils 1 and 3, in blue) and with strong basal texture (foils 2 and 4, in red) with opaque GBs under plane strain. The solid lines correspond to the foils without fracture, and the dashed lines correspond to the foils with fracture. (b) Relative contribution of the basal, prismatic, and pyramidal slip systems to the accumulated plastic slip γ as a function of the crystallographic texture in Mg thin foils 1 (random orientations, solid lines) and 2 (basal texture, dashed lines) with fully opaque GBs under plane strain conditions.

The influence of the different GB features on the strain for damage initiation ε^0_{dmg} was also analyzed in the HCP Mg foils with basal texture (foils 2 and 4). The analyzed GB features

were again α_x, L_{GB}, Θ, and n_{Trs}, together with the mean slip activation factors for basal, prismatic, and pyramidal slip, $\overline{SA}_b$, $\overline{SA}_p$, and $\overline{SA}_{py}$. The dataset for the Mg foils with basal texture (foils 2 and 4) is composed of 3102 fractured GBs for the four analyzed thin foils, classified as 1543 under plane stress and 1559 under plane strain. The Pearson correlation matrices for plane stress and plane strain are presented in Fig. 7.23, which display the influence of the GB features on ε^0_{dmg}.

Figure 7.23: Pearson correlation matrix for GB fracture in the Mg foils with strong basal texture. (a) Plane stress, (b) plane strain.

The damage analysis for the simulations under plane stress indicated that the angle α_x presents a moderate negative correlation with ε^0_{dmg}, which means that GBs that are perpendicular to the loading axis are prone to damage at lower strains. This correlation is slightly stronger than in the case of the foils with random orientations. The misorientation angle Θ, and $\overline{SA}_{py}$ show a near-zero correlation on ε^0_{dmg}, and thus, they do not have any influence on damage nucleation. The number of transparent slip systems n_{Trs} presents a weak positive correlation with ε^0_{dmg}, higher than that observed for the foils with random orientation. This suggests that the GB character has a greater effect on damage initiation in HCP Mg in the presence of texture since grain orientations are more alike and the deformation incompatibility is reduced.

The linear correlation between $\overline{SA}_b$ with ε^0_{dmg} for the foils with basal texture is smaller than for the foils with random texture, whereas the r value for $\overline{SA}_p$ remains the same. In this case, the Pearson coefficients of the basal and the prismatic slip activation factors are nearly identical but with opposite signs, with negative Pearson correlation for $\overline{SA}_b$ and positive for $\overline{SA}_p$. This is in agreement with the geometry of the hexagonal lattice because

basal and prismatic planes are perpendicular, and when one is well-oriented for slip, the other is not. According to them, damage at GBs occurs earlier when the grains across a GB are well-oriented for basal slip ($\overline{\mathrm{SA}}_{\mathrm{b}}$ is high), and conversely, damage nucleation is delayed if the grains are well-oriented for prismatic slip. Unlike the foils with random orientations, the GB length L_{GB} also presents a weak negative correlation with ε^0_{dmg}, comparable to that observed for the slip activation factors for basal and prismatic slip.

This analysis was also performed for the foils under plane strain, and the results are similar to those observed for the foils with random texture. A stronger (but moderate) correlation is observed for α_x, slightly higher than in the case of plane stress. Furthermore, the slip activation factor for basal slip $\overline{\mathrm{SA}}_{\mathrm{b}}$ presents a greater (but still very weak) correlation, whereas $\overline{\mathrm{SA}}_{\mathrm{p}}$ has no influence on ε^0_{dmg} as compared to plane stress. Apart from this, the effect of the other GB features on damage initiation is nearly identical to those presented for plane stress, with the slip activation factors for basal and prismatic and the number of transparent slip systems presenting some correlation with damage nucleation.

7.6 Conclusions

The tensile deformation of FCC Al and HCP Mg thin foils, including intergranular fracture at GBs, was simulated by means of a dislocation-based crystal plasticity model that allows for slip transfer. Intergranular fracture was introduced through cohesive surfaces governed by a bilinear traction-separation law. Polycrystalline foils with columnar grains with different textures were generated, and the effect of GB character on intergranular fracture was assessed by considering three types of simulations: foils with fully opaque GBs, foils with fully transparent GBs, and foils with translucent GBs where slip transfer is allowed when $m' > 0.8$. Two loading cases were used for each foil: plane stress and plane strain. The tensile stress-strain curves and the analysis of the onset of damage at the GB database led to the following conclusions:

- The microstructural features that influence damage initiation in FCC Al thin foils are the angle between the GB and the loading axis α_x and the number of transparent slip systems $\mathrm{n}_{\mathrm{Trs}}$, i.e., GBs perpendicular or nearly perpendicular to the loading axis and that opaque from the viewpoint of slip transfer will be damaged earlier during deformation. In the case of HCP Mg, damage nucleation is also dominated by the GB angle with the loading axis α, but the slip activation factor of the GBs also plays an important role. Thus, GBs nearly perpendicular to the loading direction whose neighboring grains are suitably oriented for basal slip will probably initiate damage. Unlike FCC Al, the HCP Mg simulations proved to be less sensitive to the GB character (fully opaque, translucent, or fully transparent GBs).
- GB character (opaque, translucent, or transparent GBs) has an important effect on damage nucleation in Al. Opaque GBs, in which dislocation pile-ups are formed, are more prone to present premature damage nucleation than translucent or transparent GBs, in which damage is delayed. Damage also propagates faster when GBs are opaque than when GBs are transparent. On the contrary, GB character has limited influence on damage nucleation in HCP Mg because stress concentrations at

GBs (that lead to damage nucleation) are controlled in HCP Mg by the anisotropic behavior of grains with different orientations.

- The loading conditions (either plane stress or plane strain) also influence the onset and propagation of intergranular damage. GB fracture under plane stress conditions depends more on the GB character (fully opaque, translucent, or fully transparent GBs), whereas the microstructural features (the angle between GB and loading axis, or the slip activation factor) are more relevant in the case of plane strain. This latter behavior is attributed to constraint induced by the plane strain condition that forces the deformation to occur in the foil plane and increases the triaxiality.
- Texture has a remarkable effect on the deformation of Mg thin foils due to their plastic anisotropy, especially on the slip system contribution to the accumulated plastic slip. Basal slip was dominant over prismatic and pyramidal slip when in the presence of random texture. Conversely, the presence of a strong basal texture promoted the activation of the better-oriented prismatic slip systems despite its greater CRSS. This led to a competitive process with the conjoint activation of both slip systems, one that is energetically favorable (basal) against one that is geometrically favorable (prismatic). In all cases, the contribution of pyramidal slip was negligible ($< 10\%$) owing to its high CRSS.

8

Conclusions and future work

8.1 Conclusions

The thesis has analyzed the mechanisms of dislocation/grain boundary interaction in metallic polycrystals from the experimental and simulation viewpoints. The experimental characterization was carried out using state-of-the-art techniques (including slip trace analysis in combination with electron backscatter diffraction, diffraction contrast tomography, and high-resolution digital image correlation) to assess the validity of different geometrical criteria to predict dislocation slip transfer/blocking at grain boundaries in FCC (Ni) and HCP (Ti) polycrystals. The best criteria were implemented in a physically-based crystal plasticity model to predict the effect of grain boundaries (and, thus, of the grain size) on the strength of metallic polycrystals taking into account the existence of different types of grain boundaries from the viewpoint of slip transmission: transparent, translucent and opaque. In addition, intergranular fracture was included in the simulations through cohesive surfaces along the grain boundaries to understand the influence of the microstructure on the nucleation and growth of damage in polycrystals.

The main conclusions of this thesis are the following:

- Slip transfer at coherent and incoherent annealing twin boundaries in pure Ni is controlled by the residual Burgers vector and takes place when $\Delta b \approx 0$, regardless of the angle between slip normals and the twist angle between the incoming and outgoing slip planes. Moreover, slip transfer seems to be controlled by dislocation cross-slip in this case. Slip transfer across regular grain boundaries is very likely to occur across low-angle regular GBs if the Luster–Morris parameter $m' > 0.8$, and it is unlikely to take place otherwise. However, there is a significant number of slip blocking instances when $0.75 < m' < 0.9$. They could be due to an error induced by the assumption that the active slip system is the one with the highest Schmid factor or to a large value of the twist angle θ, which is not known because there was no information about the grain boundary orientation within the sample.
- Laboratory-scale Diffraction Contrast tomography technique is able to provide detailed information about the microstructure (grain size, shape, and orientation as

well as grain boundary orientation) of pure Ti foils in 3D prior to deformation. The data obtained by laboratory-scale diffraction contrast tomography are of similar quality to those obtained on the sample surface by electron backscatter diffraction on the sample surface for grains > 50 μm.

- Prismatic-to prismatic slip transfer in Ti occurs when $\Delta b/b < 0.43$ or $m' > 0.8$ and both geometrical criteria give an F1 score of 0.993. They were associated with low-angle grain boundaries and with good alignment between the incoming and outgoing slip directions and slip planes. Surprisingly, the twist angle θ did not play a clear role in slip transfer/blocking and, thus, the LRB geometrical criteria was not a good predictor of slip transfer/blocking at grain boundaries. Thus, geometrical criteria based on $\Delta b/b$ or m' can be confidently used in crystal plasticity simulations to account for slip transfer/blocking at grain boundaries.
- Nevertheless, slip transfer/blocking in a few grain boundaries in Ti did not follow the geometrical criteria indicated in the previous point. Their behavior was studied as a function of the applied strain by means of high-resolution digital image correlation to take into account the effect of the local stress near GBs on slip transfer. It was found that slip transfer between a pair of well-oriented slip systems can be impeded (leading to either partial slip transfer or even blocking) if there is another dominant slip system that is more favorable in terms of the Schmid factor to accommodate the plastic deformation across the boundary. In addition, slip transfer between well-aligned slip systems across the boundary can be blocked as a result of the lack of driving force to transfer deformation due to the strain heterogeneity in the microstructure. Finally, slip transfer may occur across a highly misoriented grain boundary due to the local stress concentrations, which provide sufficient driving force to overcome the energy barrier induced by the grain boundary and transmit dislocations to the adjacent grain.
- The experimental Hall-Petch effect on FCC (Al, Cu, Ni, Ag) and HCP (Ti, Mg) polycrystals can be captured by means of computational homogenization of a representative volume element of the microstructure through a crystal plasticity model that accounts for slip transfer/blocking at grain boundaries through geometrical criteria. This result opens the path to include size effects in crystal plasticity simulations without the need for (computationally) costly strain gradient plasticity formulations.
- Numerical simulations of thin foils of FCC Al polycrystals with columnar microstructures showed that damage by grain boundary fracture is triggered at lower strains when the grain boundary is oriented perpendicularly to the loading axis and slip transfer is blocked, leading to the formation of stress concentrations. In the case of HCP Mg polycrystals, the main microstructural parameters controlling damage nucleation were the orientation of the grain boundary with respect to the loading axis (as in FCC) and the crystallographic orientation of the grains, and those grain boundaries where the adjacent grains were well-oriented for basal slip were more prone to fracture.

8.2 Future Work

Future work will be focused on the application of the presented methodologies to investigate the effect of slip transfer in other scenarios and complement the acquired information. The following lines of work are proposed:

1. The effect of the twist angle on the occurrence of slip transfer/blocking across annealing twin boundaries in pure Ni could be effectively addressed through slip trace analysis and electron backscatter diffraction because of the twin-matrix crystallographic relationship. However, this analysis should be extended to regular grain boundaries through the application of diffraction contrast tomography (to obtain the grain boundary inclination through the sample), high-resolution digital image correlation, and electron backscatter diffraction to determine the actual active slip systems.

2. The crystallographic texture of the Ti thin foils only analyzed the effect of geometrical criteria to predict prismatic-to-prismatic slip transfer. It would be interesting to extend the methodology to other samples with different grain sizes and random textures to validate or disprove the geometrical criteria for basal-to-basal and pyramidal-to-pyramidal slip transfer as well as for slip transfer between different slip systems. In particular, it would be important to assess the effect of the twist angle on these cases.

3. Use the 3D information of the microstructure of one Ti sample obtained by diffraction contrast tomography to create a model of the microstructure. The mechanical deformation of the sample will be simulated using the crystal plasticity model, including the effect of slip transfer/blocking at grain boundaries, and compared with experimental data: the macroscopic stress-strain curve as well as the deformation fields on the sample surface obtained by high-resolution digital image correlation. This task will close the experimental/simulation loop and will also shed light on the mechanisms of slip transfer/blocking in grain boundaries that do not fulfill the geometrical criteria.

4. Create 3D representative volume elements of different metals with different microstructures (grain size, texture, etc.) and carry out numerical simulations of the mechanical behavior in tension, including slip transfer/blocking at grain boundaries as well as grain boundary fracture. The simulations will provide information about the nucleation and growth of grain boundary damage that will be used to train a machine learning model that should be able to identify the local microstructural features that trigger intergranular damage during deformation. This information will be useful in designing novel microstructures that have optimum damage tolerance to intergranular cracking

Bibliography

[1] W. V. Aarle, W. Ludwig, A. King, and D. Penumadu, "An accurate projection model for diffraction image formation and inversion using a polychromatic cone beam", Journal of Applied Crystallography **48**, 334 (2015).

[2] W. Z. Abuzaid, M. D. Sangid, J. D. Carroll, H. Sehitoglu, and J. Lambros, "Slip transfer and plastic strain accumulation across grain boundaries in hastelloy x", Journal of the Mechanics and Physics of Solids **60**, 1201 (2012).

[3] W. Z. Abuzaid, H. Sehitoglu, and J. Lambros, "Localisation of plastic strain at the microstructurlal level in hastelloy x subjected to monotonic, fatigue, and creep loading: the role of grain boundaries and slip transmission", Materials at High Temperatures **33**, 384 (2016).

[4] A. Acharya and A. J. Beaudoin, "Grain-size effect in viscoplastic polycrystals at moderate strains", Journal of the Mechanics and Physics of Solids **48**, 2213 (2000).

[5] E. Alabort, D. Barba, S. Sulzer, M. Lißner, N. Petrinic, and R. C. Reed, "Grain boundary properties of a nickel-based superalloy: characterisation and modelling", Acta Materialia **151**, 377 (2018).

[6] A. Alankar, P. Eisenlohr, and D. Raabe, "A dislocation density-based crystal plasticity constitutive model for prismatic slip in α-titanium", Acta Materialia **59**, 7003 (2011).

[7] R. Alizadeh, M. Peña-Ortega, T. R. Bieler, and J. LLorca, "A criterion for slip transfer at grain boundaries in al", Scripta Materialia **178**, 408 (2020).

[8] A. Arsenlis and D. M. Parks, "Modeling the evolution of crystallographic dislocation density in crystal plasticity", Journal of the Mechanics and Physics of Solids **50**, 1979 (2002).

[9] M. F. Ashby, "The deformation of plastically non-homogeneous materials", The Philosophical Magazine: A Journal of Theoretical Experimental and Applied Physics **21**, 399 (1970).

[10] M. Atkinson, R. Thomas, A. Harte, P. Crowther, and J. Q. da Fonseca, *Defdap: deformation data analysis in python - v0.92*, 2020.

[11] J. A. El-Awady, "Unravelling the physics of size-dependent dislocation-mediated plasticity", Nature Communications 2015 6:1 **6**, 1 (2015).
[12] U. Ayachit, *The paraview guide: a parallel visualization application* (Kitware, Inc., 2015).
[13] F. Bachmann, H. Bale, N. Gueninchault, C. Holzner, and E. M. Lauridsen, "3d grain reconstruction from laboratory diffraction contrast tomography", J Appl Crystallogr **52**, 643 (2019).
[14] F. Bachmann, R. Hielscher, and H. Schaeben, "Texture analysis with mtex- free and open source software toolbox", Solid State Phenomena **160**, 63 (2010).
[15] F. Bachmann, R. Hielscher, and H. Schaeben, "Grain detection from 2d and 3d ebsd data–specification of the mtex algorithm", Ultramicroscopy **111**, 1720 (2011).
[16] G. I. Barenblatt, "The mathematical theory of equilibrium cracks in brittle fracture", Advances in Applied Mechanics **7**, 55 (1962).
[17] S. Bargmann, M. Ekh, K. Runesson, and B. Svendsen, "Modeling of polycrystals with gradient crystal plasticity: a comparison of strategies", Philosophical Magazine **90**, 1263 (2010).
[18] C. M. Barr, E. Y. Chen, J. E. Nathaniel, P. Lu, D. P. Adams, R. Dingreville, B. L. Boyce, K. Hattar, and D. L. Medlin, "Irradiation-induced grain boundary facet motion: in situ observations and atomic-scale mechanisms", Science Advances **8**, 900 (2022).
[19] E. Bayerschen, A. T. McBride, B. D. Reddy, and T. Böhlke, "Review on slip transmission criteria in experiments and crystal plasticity models", Journal of Materials Science **51**, 2243 (2016).
[20] C. J. Bayley, W. A. M. Brekelmans, and M. G. D. Geers, "A three-dimensional dislocation field crystal plasticity approach applied to miniaturized structures", Philosophical Magazine **87**, 1361 (2007).
[21] S. Bechtle, M. Kumar, B. P. Somerday, M. E. Launey, and R. O. Ritchie, "Grain-boundary engineering markedly reduces susceptibility to intergranular hydrogen embrittlement in metallic materials", Acta Materialia **57**, 4148 (2009).
[22] N. Bertin, L. Capolungo, and I. J. Beyerlein, "Hybrid dislocation dynamics based strain hardening constitutive model", International Journal of Plasticity **49**, 119 (2013).
[23] N. Bertin, C. N. Tomé, I. J. Beyerlein, M. R. Barnett, and L. Capolungo, "On the strength of dislocation interactions and their effect on latent hardening in pure magnesium", International Journal of Plasticity **62**, 72 (2014).
[24] T. R. Bieler, R. Alizadeh, M. Peña-Ortega, and J. Llorca, "An analysis of (the lack of) slip transfer between near-cube oriented grains in pure al", International Journal of Plasticity **118**, 269 (2019).
[25] T. R. Bieler, P. Eisenlohr, F. Roters, D. Kumar, D. E. Mason, M. A. Crimp, and D. Raabe, "The role of heterogeneous deformation on damage nucleation at grain boundaries in single phase metals", International Journal of Plasticity **25**, 1655 (2009).
[26] T. R. Bieler, S. C. Sutton, B. E. Dunlap, Z. A. Keith, P. Eisenlohr, M. A. Crimp, and B. L. Boyce, "Grain boundary responses to heterogeneous deformation in tantalum polycrystals", JOM **66**, Bieler, slip transfer in Ta BCC using m', 121 (2014).
[27] B. R. Blackman, H. Hadavinia, A. J. Kinloch, and J. G. Williams, "The use of a cohesive zone model to study the fracture of fibre composites and adhesively-bonded joints", International Journal of Fracture **119**, 25 (2003).

[28] N. Bozzolo and M. Bernacki, "Viewpoint on the formation and evolution of annealing twins during thermomechanical processing of fcc metals and alloys", Metallurgical and Materials Transactions A 2020 51:6 **51**, 2665 (2020).
[29] V. V. Bulatov, B. W. Reed, and M. Kumar, "Grain boundary energy function for fcc metals", 10.1016/j.actamat.2013.10.057 (2013).
[30] W. D. Callister, *Fundamentals of materials science and engineering*, Vol. 471660817 (Wiley, 2000), pp. 115–117.
[31] P. P. Camanho and C. G. Davila, *Mixed-mode decohesion finite elements for the simulation of delamination in composite materials*, 2002.
[32] R. D. Campilho, M. D. Banea, J. A. Neto, and L. F. D. Silva, "Modelling adhesive joints with cohesive zone models: effect of the cohesive law shape of the adhesive layer", International Journal of Adhesion and Adhesives **44**, 48 (2013).
[33] R. P. Carreker, "Tensile deformation of silver as a function of temperature, strain rate, and grain size", The Journal of The Minerals, Metals & Materials Society (JOM-TMS) **9**, 112 (1957).
[34] C. M. Cepeda-Jiménez, J. M. Molina-Aldareguia, and M. T. Pérez-Prado, "Origin of the twinning to slip transition with grain size refinement, with decreasing strain rate and with increasing temperature in magnesium", Acta Materialia **88**, 232 (2015).
[35] C. M. Cepeda-Jiménez, J. M. Molina-Aldareguia, and M. T. Pérez-Prado, "Ebsd-assisted slip trace analysis during in situ sem mechanical testing: application to unravel grain size effects on plasticity of pure mg polycrystals", JOM **68**, 116 (2016).
[36] A. Chapuis and J. H. Driver, "Temperature dependency of slip and twinning in plane strain compressed magnesium single crystals", Acta Materialia **59**, 1986 (2011).
[37] R. Chatterjee and A. A. Alankar, "Crystal plasticity modeling of dynamic recrystallization in cp ti", in , Vol. 14 (2019), pp. 251–258.
[38] J. Chen, J. Lu, W. Cai, Y. Zhang, Y. Wang, W. Jiang, M. Rizwan, and Z. Zhang, "In-situ study of adjacent grains slip transfer of inconel 718 during tensile process at high temperature", International Journal of Plasticity **163**, 10.1016/j.ijplas.2023.103554 (2023).
[39] Z. Chen and S. H. Daly, "Active slip system identification in polycrystalline metals by digital image correlation (dic)", Experimental Mechanics **57**, 115 (2017).
[40] K. S. Cheong, E. P. Busso, and A. Arsenlis, "A study of microstructural length scale effects on the behaviour of fcc polycrystals using strain gradient concepts", International Journal of Plasticity **21**, 1797 (2005).
[41] W. Clark, R. Wagoner, Z. Shen, T. Lee, I. Robertson, and H. Birnbaum, "On the criteria for slip transmission across interfaces in polycrystals", **26**, Shen Robertson. Slip transmission FCC deltab, 203 (1992).
[42] J. D. Clayton and D. L. McDowell, "Homogenized finite elastoplasticity and damage: theory and computations", Mechanics of Materials **36**, 799 (2004).
[43] M. Dao, L. Lu, R. J. Asaro, J. T. D. Hosson, and E. Ma, "Toward a quantitative understanding of mechanical behavior of nanocrystalline metals", Acta Materialia **55**, 4041 (2007).
[44] B. Devincre, T. Hoc, and L. Kubin, "Dislocation mean free paths and strain hardening of crystals", Science **320**, 1745 (2008).

[45] S. J. Dillon and G. S. Rohrer, "Characterization of the grain-boundary character and energy distributions of yttria using automated serial sectioning and ebsd in the fib", Journal of the American Ceramic Society **92**, 1580 (2009).
[46] D. S. Dugdale, "Yielding of steel sheets containing slits", Journal of the Mechanics and Physics of Solids **8**, 100 (1960).
[47] D. J. Dunstan and A. J. Bushby, "The scaling exponent in the size effect of small scale plastic deformation", International Journal of Plasticity **40**, 152 (2013).
[48] D. J. Dunstan and A. J. Bushby, "Grain size dependence of the strength of metals: the hall–petch effect does not scale as the inverse square root of grain size", International Journal of Plasticity **53**, 56 (2014).
[49] P. D. Edmondson, Y. Zhang, S. Moll, F. Namavar, and W. J. Weber, "Irradiation effects on microstructure change in nanocrystalline ceria - phase, lattice stress, grain size and boundaries", Acta Materialia **60**, 5408 (2012).
[50] M. Elices, G. V. Guinea, J. Gómez, and J. Planas, "The cohesive zone model: advantages, limitations and challenges", Engineering Fracture Mechanics **69**, 137 (2002).
[51] U. Essmann and H. Mughrabi, "Annihilation of dislocations during tensile and cyclic deformation and limits of dislocation densities", Philosophical Magazine A **40**, 731 (1979).
[52] G. Esteban-Manzanares, R. Santos-Güemes, I. Papadimitriou, E. Martínez, and J. LLorca, "Influence of the stress state on the cross-slip free energy barrier in al: an atomistic investigation", Acta Materialia **184**, 109 (2020).
[53] L. P. Evers, D. M. Parks, W. A. M. Brekelmans, and M. G. D. Geers, "Crystal plasticity model with enhanced hardening by geometrically necessary dislocation accumulation", Journal of the Mechanics and Physics of Solids **50**, 2403 (2002).
[54] H. Fang, D. J. Jensen, and Y. Zhang, "An efficient method to improve the spatial resolution of laboratory x-ray diffraction contrast tomography", IOP Conference Series: Materials Science and Engineering **580**, 10.1088/1757-899x/580/1/012030 (2019).
[55] H. Fang, D. J. Jensen, and Y. Zhang, "Improved grain mapping by laboratory x-ray diffraction contrast tomography", IUCrJ **8**, 559 (2021).
[56] M. Feser, C. Holzner, and E. Lauridsen, *Laboratory x-ray micro-tomography system with crystallographic gran orientation mapping capabilities*, 2015.
[57] P. Franciosi, M. Berveiller, and A. Zaoui, "Latent hardening in copper and aluminium single crystals", Acta Metallurgica **28**, 273 (1980).
[58] L. H. Friedman and D. C. Chrzan, "Continuum analysis of dislocation pile-ups: influence of sources", Philosophical Magazine A **77**, 1185 (1998).
[59] B. H. Frodal, S. Thomesen, T. Børvik, and O. S. Hopperstad, "On the coupling of damage and single crystal plasticity for ductile polycrystalline materials", International Journal of Plasticity **142**, 102996 (2021).
[60] E. Ganju, E. Nieto-Valeiras, J. LLorca, and N. Chawla, "A novel diffraction contrast tomography (dct) acquisition strategy for capturing the 3d crystallographic structure of pure titanium", Tomography of Materials and Structures **1**, 100003 (2023).
[61] W. M. Garrison and N. R. Moody, "Ductile fracture", Journal of Physics and Chemistry of Solids **48**, 1035 (1987).

[62] J. Genée, L. Signor, and P. Villechaise, "Slip transfer across grain/twin boundaries in polycrystalline ni-based superalloys", Materials Science and Engineering: A **701**, 24 (2017).

[63] C. Geuzaine and J. F. Remacle, "Gmsh: a 3-d finite element mesh generator with built-in pre- and post-processing facilities", International Journal for Numerical Methods in Engineering **79**, 1309 (2009).

[64] A. Ghosh, A. Singh, and N. P. Gurao, "Effect of rolling mode and annealing temperature on microstructure and texture of commercially pure-titanium", Materials Characterization **125**, 83 (2017).

[65] F. D. Gioacchino, T. E. Edwards, G. N. Wells, and W. J. Clegg, "A new mechanism of strain transfer in polycrystals", Scientific Reports **10**, 10.1038/s41598-020-66569-7 (2020).

[66] F. D. Gioacchino and J. Q. da Fonseca, "Plastic strain mapping with sub-micron resolution using digital image correlation", Experimental Mechanics **53**, 743 (2013).

[67] J. Gong and A. J. Wilkinson, "Anisotropy in the plastic flow properties of single-crystal α titanium determined from micro-cantilever beams", Acta Materialia **57**, 5693 (2009).

[68] S. Graff, W. Brocks, and D. Steglich, "Yielding of magnesium: from single crystal to polycrystalline aggregates", International Journal of Plasticity **23**, 1957 (2007).

[69] M. A. Groeber and M. A. Jackson, *Dream.3d: a digital representation environment for the analysis of microstructure in 3d*, 2014.

[70] Y. Guo, T. B. Britton, and A. J. Wilkinson, "Slip band-grain boundary interactions in commercial-purity titanium", Acta Materialia **76**, 1 (2014).

[71] Y. Guo, D. M. Collins, E. Tarleton, F. Hofmann, J. Tischler, W. Liu, R. Xu, A. J. Wilkinson, and T. B. Britton, "Measurements of stress fields near a grain boundary: exploring blocked arrays of dislocations in 3d", Acta Materialia **96**, 229 (2015).

[72] E. O. Hall, "The deformation and ageing of mild steel: ii characteristics of the lüders deformation", Proceedings of the Physical Society. Section B **64**, 742 (1951).

[73] S. Han and M. A. Crimp, "Ecci analysis of shear accommodations at grain boundaries in commercially pure alpha titanium", International Journal of Plasticity **131**, 10.1016/j.ijplas.2020.102731 (2020).

[74] N. Hansen, "The effect of grain size and strain on the tensile flow stress of aluminium at room temperature", Acta Metallurgica **25**, 863 (1977).

[75] N. Hansen and B. Ralph, "The strain and grain size dependence of the flow stress of copper", Acta Metallurgica **30**, 411 (1982).

[76] S. Haouala, R. Alizadeh, T. R. Bieler, J. Segurado, and J. Llorca, "Effect of slip transmission at grain boundaries in al bicrystals", International Journal of Plasticity **126**, 10.1016/j.ijplas.2019.09.006 (2020).

[77] S. Haouala, S. Lucarini, J. LLorca, and J. Segurado, "Simulation of the hall-petch effect in fcc polycrystals by means of strain gradient crystal plasticity and fft homogenization", Journal of the Mechanics and Physics of Solids **134**, 10.1016/j.jmps.2019.103755 (2020).

[78] S. Haouala, J. Segurado, and J. LLorca, "An analysis of the influence of grain size on the strength of fcc polycrystals by means of computational homogenization", Acta Materialia **148**, 72 (2018).

[79] A. Harte, M. Atkinson, M. Preuss, and J. Q. da Fonseca, "A statistical study of the relationship between plastic strain and lattice misorientation on the surface of a deformed ni-based superalloy", Acta Materialia **195**, 555 (2020).
[80] A. Harte, M. Atkinson, A. Smith, C. Drouven, S. Zaefferer, J. Q. da Fonseca, and M. Preuss, "The effect of solid solution and gamma prime on the deformation modes in ni-based superalloys", Acta Materialia **194**, 257 (2020).
[81] R. F. S. Hearmon, "The elastic constants of crystals and other anisotropic materials", Landolt-Börnstein Tables **3**, 559 (1984).
[82] S. Hémery, P. Nizou, and P. Villechaise, "In situ sem investigation of slip transfer in ti-6al-4v: effect of applied stress", Materials Science and Engineering: A **709**, 277 (2018).
[83] J. P. Hirth, "Influence of grain boundaries on mechanical properties.", Metall Trans **3**, 3047 (1972).
[84] C. Holzner, L. Lavery, H. Bale, A. Merkle, S. McDonald, P. Withers, Y. Zhang, D. J. Jensen, M. Kimura, A. Lyckegaard, P. Reischig, and E. M. Lauridsen, "Diffraction contrast tomography in the laboratory – applications and future directions", Microscopy Today **24**, 34 (2016).
[85] D. A. Hughes, N. Hansen, and D. J. Bammann, "Geometrically necessary boundaries, incidental dislocation boundaries and geometrically necessary dislocations", Scripta Materialia **48**, 147 (2003).
[86] D. Hull and D. Bacon, *Introduction to dislocations*, Fifth Edition, Vol. 37 (Elsevier, 2011).
[87] A. Jamali, A. Ma, and J. LLorca, "Influence of grain size and grain boundary misorientation on the fatigue crack initiation mechanisms of textured az31 mg alloy", Scripta Materialia **207**, 114304 (2022).
[88] S. Jiang, Y. Jia, and X. Wang, "In-situ analysis of slip transfer and heterogeneous deformation in tension of mg-5.4gd-1.8y-1.5zn alloy", Journal of Magnesium and Alloys **8**, 1186 (2020).
[89] G. Johnson, A. King, M. G. Honnicke, J. Marrow, and W. Ludwig, "X-ray diffraction contrast tomography: a novel technique for three-dimensional grain mapping of polycrystals. ii. the combined case", Journal of Applied Crystallography **41**, 310 (2008).
[90] R. Jones, "Stress-corrosion cracking", in , Vol. 13A (ASM International, 2003), pp. 346–366.
[91] J. Kacher, B. P. Eftink, B. Cui, and I. M. Robertson, "Dislocation interactions with grain boundaries", Current Opinion in Solid State and Materials Science **18**, 227 (2014).
[92] R. Keinan, H. Bale, N. Gueninchault, E. M. Lauridsen, and A. J. Shahani, "Integrated imaging in three dimensions: providing a new lens on grain boundaries, particles, and their correlations in polycrystalline silicon", Acta Materialia **148**, 225 (2018).
[93] A. King, P. Reischig, J. Adrien, and W. Ludwig, "First laboratory x-ray diffraction contrast tomography for grain mapping of polycrystals", Journal of Applied Crystallography **46**, 1734 (2013).

[94] K. Kishida, J. G. Kim, T. Nagae, and H. Inui, "Experimental evaluation of critical resolved shear stress for the first-order pyramidal c+a slip in commercially pure ti by micropillar compression method", Acta Materialia **196**, 168 (2020).
[95] S. Kobayashi, S. Ogou, and S. Tsurekawa, "Grain boundary engineering for control of fatigue fracture in 316l austenitic stainless steel", Materials Transactions **60**, 623 (2019).
[96] U. F. Kocks, "The relation between polycrystal deformation and single-crystal deformation", Metallurgical and Materials Transactions **1**, 1121 (1970).
[97] U. F. Kocks, A. S. Argon, and M. F. Ashby, *Thermodynamics and kinetics of slip*, Vol. 19 (Pergamon press, 1975).
[98] U. F. Kocks and H. Mecking, "Physics and phenomenology of strain hardening: the fcc case", Progress in Materials Science **48**, 171 (2003).
[99] V. Kotu and B. Deshpande, "Data exploration", in , Second Edition (Morgan Kaufmann, Jan. 2019), pp. 39–64.
[100] L. P. Kubin, *Dislocations, mesoscale simulations and plastic flow*, First, Vol. 5 (Oxford University Press, 2013).
[101] K. S. Kumar, H. V. Swygenhoven, and S. Suresh, "Mechanical behavior of nanocrystalline metals and alloys", Acta Materialia **51**, 5743 (2003).
[102] M. A. Kumar, I. J. Beyerlein, R. A. Lebensohn, and C. N. Tomé, "Modeling the effect of neighboring grains on twin growth in hcp polycrystals", Modelling and Simulation in Materials Science and Engineering **25**, 064007 (2017).
[103] B. Larrouy, P. Villechaise, J. Cormier, and O. Berteaux, "Grain boundary–slip bands interactions: impact on the fatigue crack initiation in a polycrystalline forged ni-based superalloy", Acta Materialia **99**, 325 (2015).
[104] LaVision, *Davis software for intelligent imaging*, 2020.
[105] R. A. Lebensohn and A. Needleman, "Numerical implementation of non-local polycrystal plasticity using fast fourier transforms", Journal of the Mechanics and Physics of Solids **97**, 333 (2016).
[106] J. S. Lecomte, L. T. Nguyen, F. Abbès, C. Schuman, and J. M. Raulot, "Contribution of the nanoindentation to the study of hcp metals", Materials Science Forum **783-786**, 2327 (2014).
[107] R. J. Lederich, S. M. L. Sastry, J. E. O'neal, and B. B. Rath, "The effect of grain size on yield stress and work hardening of polycrystalline titanium at 295 k and 575 k", Materials Science and Engineering **33**, 183 (1978).
[108] T. C. Lee, I. M. Robertson, and H. K. Birnbaum, "Prediction of slip transfer mechanisms across grain boundaries", Scripta Metallurgica **23**, 799 (1989).
[109] T. C. Lee, I. M. Robertson, and H. K. Birnbaum, "Anin situ transmission electron microscope deformation study of the slip transfer mechanisms in metals", Metallurgical Transactions A **21**, 2437 (1990).
[110] S. F. Li and R. M. Suter, "Adaptive reconstruction method for three-dimensional orientation imaging", Journal of Applied Crystallography **46**, 512 (2013).
[111] S. Li, M. D. Thouless, A. M. Waas, J. A. Schroeder, and P. D. Zavattieri, "Use of a cohesive-zone model to analyze the fracture of a fiber-reinforced polymer–matrix composite", Composites Science and Technology **65**, 537 (2005).

[112] Y. Li, A. J. Bushby, and D. J. Dunstan, "The hall–petch effect as a manifestation of the general size effect", Proceedings of the Royal Society A: Mathematical, Physical and Engineering Sciences **472**, 10.1098/RSPA.2015.0890 (2016).
[113] D. Liang, J. Hure, A. Courcelle, S. E. Shawish, and B. Tanguy, "A micromechanical analysis of intergranular stress corrosion cracking of an irradiated austenitic stainless steel", Acta Materialia **204**, 116482 (2021).
[114] L. C. Lim and R. Raj, "The role of residual dislocation arrays in slip induced cavitation, migration and dynamic recrystallization at grain boundaries", Acta Metallurgica **33**, 2205 (1985).
[115] J. D. Livingston and B. Chalmers, "Multiple slip in bicrystal deformation", Acta Metallurgica **5**, 322 (1957).
[116] W. Ludwig, P. Reischig, A. King, M. Herbig, E. M. Lauridsen, G. Johnson, T. J. Marrow, and J. Y. Buffiere, "Three-dimensional grain mapping by x-ray diffraction contrast tomography and the use of friedel pairs in diffraction data analysis", Rev Sci Instrum **80**, 33905 (2009).
[117] W. Ludwig, S. Schmidt, E. M. Lauridsen, and H. F. Poulsen, "X-ray diffraction contrast tomography: a novel technique for three-dimensional grain mapping of polycrystals. i. direct beam case", Journal of Applied Crystallography **41**, 302 (2008).
[118] J. Luster and M. A. Morris, "Compatibility of deformation in two-phase ti-al alloys: dependence on microstructure and orientation relationships", Metallurgical and Materials Transactions A **26**, 1745 (1995).
[119] G. Martin, C. W. Sinclair, and R. A. Lebensohn, "Microscale plastic strain heterogeneity in slip dominated deformation of magnesium alloy containing rare earth", Materials Science and Engineering: A **603**, 37 (2014).
[120] R. S. Martín, J. M. Molina-Aldareguia, and M. T. P. Prado, "Micromechanics of magnesium and its alloys studied by nanoindentation", (2016).
[121] E. Martínez-Pañeda and C. Betegón, "Modeling damage and fracture within strain-gradient plasticity", International Journal of Solids and Structures **59**, 208 (2015).
[122] S. A. McDonald, C. Holzner, E. M. Lauridsen, P. Reischig, A. P. Merkle, and P. J. Withers, "Microstructural evolution during sintering of copper particles studied by laboratory diffraction contrast tomography (labdct)", Sci Rep **7**, 5251 (2017).
[123] S. A. McDonald, P. Reischig, C. Holzner, E. M. Lauridsen, P. J. Withers, A. P. Merkle, and M. Feser, "Non-destructive mapping of grain orientations in 3d by laboratory x-ray microscopy", Sci Rep **5**, 14665 (2015).
[124] S. A. McDonald, T. L. Burnett, J. Donoghue, N. Gueninchault, H. Bale, C. Holzner, E. M. Lauridsen, and P. J. Withers, "Tracking polycrystal evolution non-destructively in 3d by laboratory x-ray diffraction contrast tomography", Materials Characterization **172**, 10.1016/j.matchar.2020.110814 (2021).
[125] C. J. McMahon, "Intergranular fracture in steels", Materials Science and Engineering **25**, 233 (1976).
[126] M. D. McMurtrey, B. Cui, I. Robertson, D. Farkas, and G. S. Was, "Mechanism of dislocation channel-induced irradiation assisted stress corrosion crack initiation in austenitic stainless steel", Current Opinion in Solid State and Materials Science **19**, 305 (2015).

[127] T. Narutani and J. Takamura, "Grain-size strengthening in terms of dislocation density measured by resistivity", Acta Metallurgica et Materialia **39**, 2037 (1991).
[128] S. Nemat-Nasser, W. G. Guo, and J. Y. Cheng, "Mechanical properties and deformation mechanisms of a commercially pure titanium", Acta materialia **47**, 3705 (1999).
[129] M. G. Nicholas and C. F. Old, "Liquid metal embrittlement", Journal of Materials Science **14**, 1 (1979).
[130] E. Nieto-Valeiras and J. LLorca, "Criteria for slip transfer across grain and twin boundaries in pure ni", Materialia **21**, 10.1016/j.mtla.2021.101303 (2022).
[131] E. Nieto-Valeiras, E. Ganju, N. Chawla, and J. LLorca, "Assessment of slip transfer criteria for prismatic-to-prismatic slip in pure ti from 3d grain boundary data", Acta Materialia **262**, 119424 (2024).
[132] S. Niverty, J. Sun, J. Williams, F. Bachmann, N. Gueninchault, E. Lauridsen, and N. Chawla, "A forward modeling approach to high-reliability grain mapping by laboratory diffraction contrast tomography (labdct)", JOM **71**, 2695 (2019).
[133] J. F. Nye, "Some geometrical relations in dislocated crystals", Acta Metallurgica **1**, 153 (1953).
[134] J. Oddershede, F. Bachmann, J. Sun, and E. Lauridsen, "Advanced acquisition strategies for lab-based diffraction contrast tomography", Integrating Materials and Manufacturing Innovation **11**, 1 (2022).
[135] N. Ono, R. Nowak, and S. Miura, "Effect of deformation temperature on hall–petch relationship registered for polycrystalline magnesium", Materials Letters **58**, 39 (2004).
[136] A. Orozco-Caballero, D. Lunt, J. D. Robson, and J. Q. da Fonseca, "How magnesium accommodates local deformation incompatibility: a high-resolution digital image correlation study", Acta Materialia **133**, 367 (2017).
[137] G. Palumbo, D. Dunikowski, R. Wirecka, T. Mazur, U. Lelek-Borkowska, K. Wawer, and J. Banas, "Effect of grain size on the corrosion behavior of fe-3wt.%si-1wt.%al electrical steels in pure water saturated with co(2)", Materials (Basel) **14**, 10.3390/ma14175084 (2021).
[138] H. Pan, Y. He, and X. Zhang, "Interactions between dislocations and boundaries during deformation", Materials 2021, Vol. 14, Page 1012 **14**, 1012 (2021).
[139] K. Park and G. H. Paulino, "Cohesive zone models: a critical review of traction-separation relationships across fracture surfaces", Applied Mechanics Reviews **64**, 10.1115/1.4023110 (2011).
[140] L. Patriarca, W. Abuzaid, H. Sehitoglu, and H. J. Maier, "Slip transmission in bcc fecr polycrystal", Materials Science and Engineering A **588**, Slip transfer studied in BCC by HRDIC. They use the residual Burgers vector as criterion, and it works as usual., 308 (2013).
[141] P. Pauš, J. Kratochvíl, and M. Beneš, "A dislocation dynamics analysis of the critical cross-slip annihilation distance and the cyclic saturation stress in fcc single crystals at different temperatures", Acta Materialia **61**, 7917 (2013).
[142] J. Pelleg, *Mechanical properties of materials*, 1st ed. (Springer, 2013).
[143] N. J. Petch, "The cleavage strength of polycrystals", J. Iron Steel Inst. **174**, 25 (1953).

[144] H. Pirgazi, K. Glowinski, A. Morawiec, and L. A. I. Kestens, "Three-dimensional characterization of grain boundaries in pure nickel by serial sectioning via mechanical polishing", Journal of Applied Crystallography **48**, 1672 (2015).
[145] D. M. W. Powers, "Evaluation: from precision, recall and f-measure to roc, informedness, markedness and correlation", International Journal of Machine Learning Technology, 37 (2011).
[146] R. Quey, P. R. Dawson, and F. Barbe, "Large-scale 3d random polycrystals for the finite element method: generation, meshing and remeshing", Computer Methods in Applied Mechanics and Engineering **200**, 1729 (2011).
[147] S. V. Raj and G. M. Pharr, "A compilation and analysis of data for the stress dependence of the subgrain size", Materials Science and Engineering **81**, 217 (1986).
[148] K. D. Ralston, N. Birbilis, and C. H. J. Davies, "Revealing the relationship between grain size and corrosion rate of metals", Scripta Materialia **63**, 1201 (2010).
[149] W. T. Read and W. Shockley, "Dislocation models of crystal grain boundaries", Physical Review **78**, 275 (1950).
[150] I. M. Robertson, T. Tabata, W. Wei, F. Heubaum, and H. K. Birnbaum, "Hydrogen embrittlement and grain boundary fracture", Scripta Metallurgica **18**, 841 (1984).
[151] R. A. Rubio, S. Haouala, and J. Llorca, "Grain boundary strengthening of fcc polycrystals", Journal of Materials Research **34**, 2263 (2019).
[152] R. Sánchez-Martín, M. T. Pérez-Prado, J. Segurado, J. Bohlen, I. Gutiérrez-Urrutia, J. Llorca, and J. M. Molina-Aldareguia, "Measuring the critical resolved shear stresses in mg alloys by instrumented nanoindentation", Acta Materialia **71**, 283 (2014).
[153] C. D. Sansal, B. Devincre, and L. Kubin, "Grain size strengthening in microcrystalline copper: a three-dimensional dislocation dynamics simulation", Key Engineering Materials **423**, 25 (2010).
[154] M. Sarebanzadeh, A. Orozco-Caballero, and J. Llorca, "Accurate determination of active slip systems for improved geometrical criteria of basal-to-basal slip transfer at grain boundaries in pure mg", Acta Materialia **243**, https://doi.org/10.1016/j.actamat.2022.118536 (2023).
[155] M. Sauzay and L. P. Kubin, "Scaling laws for dislocation microstructures in monotonic and cyclic deformation of fcc metals", Progress in Materials Science **56**, 725 (2011).
[156] J. Schindelin, I. Arganda-Carreras, E. Frise, V. Kaynig, M. Longair, T. Pietzsch, S. Preibisch, C. Rueden, S. Saalfeld, B. Schmid, J. Y. Tinevez, D. J. White, V. Hartenstein, K. Eliceiri, P. Tomancak, and A. Cardona, "Fiji: an open-source platform for biological-image analysis", Nature Methods **9**, 676 (2012).
[157] A. J. Schwartz, M. Kumar, B. L. Adams, and D. P. Field, *Electron backscatter diffraction in materials science* (Springer US, 2009), pp. 1–403.
[158] J. Segurado, R. A. Lebensohn, and J. Llorca, "Computational homogenization of polycrystals", Advances in Applied Mechanics **51**, 1 (2018).
[159] S. E. Shawish, L. Cizelj, and I. Simonovski, "Modeling grain boundaries in polycrystals using cohesive elements: qualitative and quantitative analysis", Nuclear Engineering and Design **261**, 371 (2013).
[160] Z. Shen, R. H. Wagoner, and W. A. T. Clark, "Dislocation and grain boundary interactions in metals", Acta Metallurgica **36**, 3231 (1988).

[161] K. Sieradzki and R. C. Newman, "Stress-corrosion cracking", Journal of Physics and Chemistry of Solids **48**, 1101 (1987).
[162] I. Simonovski and L. Cizelj, "Cohesive zone modeling of intergranular cracking in polycrystalline aggregates", Nuclear Engineering and Design **283**, 139 (2015).
[163] D. S. Simulia, *Standard user's manual and abaqus cae manual 6.14*, Vol. 1 (2006).
[164] R. E. Smallman and A. H. W. Ngan, *Surfaces, grain boundaries and interfaces* (Butterworth-Heinemann, Aug. 2014), pp. 415–442.
[165] M. Soleimani, H. Mirzadeh, and C. Dehghanian, "Effect of grain size on the corrosion resistance of low carbon steel", Materials Research Express **7**, 10.1088/2053-1591/ab62fa (2020).
[166] R. Sperry, S. Han, Z. Chen, S. H. Daly, M. A. Crimp, and D. T. Fullwood, "Comparison of ebsd, dic, afm, and ecci for active slip system identification in deformed ti-7al", Materials Characterization **173**, 10.1016/j.matchar.2021.110941 (2021).
[167] R. Sperry, A. Harte, J. Q. da Fonseca, E. R. Homer, R. H. Wagoner, and D. T. Fullwood, "Slip band characteristics in the presence of grain boundaries in nickel-based superalloy", Acta Materialia **193**, 229 (2020).
[168] J. C. Stinville, W. C. Lenthe, M. P. Echlin, P. G. Callahan, D. Texier, and T. M. Pollock, "Microstructural statistics for fatigue crack initiation in polycrystalline nickel-base superalloys", International Journal of Fracture **208**, 221 (2017).
[169] J. C. Stinville, W. C. Lenthe, J. Miao, and T. M. Pollock, "A combined grain scale elastic–plastic criterion for identification of fatigue crack initiation sites in a twin containing polycrystalline nickel-base superalloy", Acta Materialia **103**, 461 (2016).
[170] J. C. Stinville, N. Vanderesse, F. Bridier, P. Bocher, and T. M. Pollock, "High resolution mapping of strain localization near twin boundaries in a nickel-based superalloy", Acta Materialia **98**, 29 (2015).
[171] J. Sun, F. Bachmann, J. Oddershede, and E. Lauridsen, "Recent advances of lab-based diffraction contrast tomography – reconstruction speed benchmark testing and validations", IOP Conference Series: Materials Science and Engineering **1249**, /10.1088/1757-899X/1249/1/012045 (2022).
[172] J. Sun, A. Lyckegaard, Y. B. Zhang, S. A. Catherine, B. R. Patterson, F. Bachmann, N. Gueninchault, H. Bale, C. Holzner, E. Lauridsen, and D. J. Jensen, "4d study of grain growth in armco iron using laboratory x-ray diffraction contrast tomography", IOP Conference Series: Materials Science and Engineering **219**, 10.1088/1757-899x/219/1/012039 (2017).
[173] J. Sun, Y. Zhang, A. Lyckegaard, F. Bachmann, E. M. Lauridsen, and D. J. Jensen, "Grain boundary wetting correlated to the grain boundary properties: a laboratory-based multimodal x-ray tomography investigation", Scripta Materialia **163**, 77 (2019).
[174] C. Suryanarayana, "Nanocrystalline materials", International Materials Reviews **40**, 41 (1995).
[175] G. I. Taylor, "The mechanism of plastic deformation of crystals. part ii.—comparison with observations", Proceedings of the Royal Society of London. Series A **145**, 388 (1934).
[176] A. Tharwat, "Classification assessment methods", Applied Computing and Informatics **17**, 168 (2018).
[177] P. F. Thomason, *Ductile fracture of metals. pergamon press, oxford* (1990).

[178] T. Vermeij, R. H. Peerlings, M. G. Geers, and J. P. Hoefnagels, "Automated identification of slip system activity fields from digital image correlation data", Acta Materialia **243**, 118502 (2023).
[179] F. Wang, S. Sandlöbes, M. Diehl, L. Sharma, F. Roters, and D. Raabe, "In situ observation of collective grain-scale mechanics in mg and mg–rare earth alloys", Acta Materialia **80**, 77 (2014).
[180] J. Y. Wang, N. Li, R. Alizadeh, M. A. Monclús, Y. W. Cui, J. M. Molina-Aldareguía, and J. LLorca, "Effect of solute content and temperature on the deformation mechanisms and critical resolved shear stress in mg-al and mg-zn alloys", Acta Materialia **170**, 155 (2019).
[181] J. Wang, Y. Chen, Z. Chen, J. Llorca, and X. Zeng, "Deformation mechanisms of mg-ca-zn alloys studied by means of micropillar compression tests", Acta Materialia **217**, 117151 (2021).
[182] L. Wang, Y. Yang, P. Eisenlohr, T. R. Bieler, M. A. Crimp, and D. E. Mason, "Twin nucleation by slip transfer across grain boundaries in commercial purity titanium", Metallurgical and Materials Transactions A: Physical Metallurgy and Materials Science **41**, 421 (2010).
[183] L. Wang, Z. Zheng, H. Phukan, P. Kenesei, J. S. Park, J. Lind, R. M. Suter, and T. R. Bieler, "Direct measurement of critical resolved shear stress of prismatic and basal slip in polycrystalline ti using high energy x-ray diffraction microscopy", Acta Materialia **132**, 598 (2017).
[184] M. G. Wang and A. H. Ngan, "Indentation strain burst phenomenon induced by grain boundaries in niobium", Journal of Materials Research **19**, 2478 (2004).
[185] Z. M. Wang, R. M. Osgood, and J. Parisi, *Grain boundaries: from theory to engineering*, Vol. 172 (Springer, 2013).
[186] Y. J. Wei and L. Anand, "Grain-boundary sliding and separation in polycrystalline metals: application to nanocrystalline fcc metals", Journal of the Mechanics and Physics of Solids **52**, 2587 (2004).
[187] D. Xie and A. M. Waas, "Discrete cohesive zone model for mixed-mode fracture using finite element analysis", Engineering Fracture Mechanics **73**, 1783 (2006).
[188] Xnovotech, *Grainmapper 3d user's guide*, 2022.
[189] X. Xu, D. Lunt, R. Thomas, R. P. Babu, A. Harte, M. Atkinson, J. Q. D. Fonseca, and M. Preuss, "Identification of active slip mode in a hexagonal material by correlative scanning electron microscopy", 10.1016/j.actamat.2019.06.024 (2019).
[190] B. Yang, C. Shi, R. Lai, D. Shi, D. Guan, G. Zhu, Y. Cui, G. Xie, Y. Li, A. Chiba, and J. LLorca, "Identification of active slip systems in polycrystals by slip trace - modified lattice rotation analysis (st-mlra)", Scripta Materialia **214**, 10.1016/j.scriptamat.2022.114648 (2022).
[191] B. Yavuzyegit, E. Avcu, A. D. Smith, J. M. Donoghue, D. Lunt, J. D. Robson, T. L. Burnett, J. Q. da Fonseca, and P. J. Withers, "Mapping plastic deformation mechanisms in az31 magnesium alloy at the nanoscale", Acta Materialia **250**, 118876 (2023).
[192] M. Zaiser and S. Sandfeld, "Scaling properties of dislocation simulations in the similitude regime", Modelling and Simulation in Materials Science and Engineering **22**, 65012 (2014).

[193] T. Zhai, A. J. Wilkinson, and J. W. Martin, "A crystallographic mechanism for fatigue crack propagation through grain boundaries", Acta Materialia **48**, 4917 (2000).

[194] J. Zhang and S. P. Joshi, "Phenomenological crystal plasticity modeling and detailed micromechanical investigations of pure magnesium", Journal of the Mechanics and Physics of Solids **60**, 945 (2012).

[195] Z. Zhang, Z. Yang, S. Lu, A. Harte, R. Morana, and M. Preuss, "Strain localisation and failure at twin-boundary complexions in nickel-based superalloys", Nature Communications **11**, 10.1038/s41467-020-18641-z (2020).

[196] Y. Zhao, S. Niverty, X. Ma, and N. Chawla, "Correlation between corrosion behavior and grain boundary characteristics of a 6061 al alloy by lab-scale x-ray diffraction contrast tomography (dct)", Materials Characterization **193**, 10.1016/j.matchar.2022.112325 (2022).

[197] Z. Zhao, M. Ramesh, D. Raabe, A. M. Cuitiño, and R. Radovitzky, "Investigation of three-dimensional aspects of grain-scale plastic surface deformation of an aluminum oligocrystal", International Journal of Plasticity **24**, 2278 (2008).

[198] Z. Zhao, T. R. Bieler, J. LLorca, and P. Eisenlohr, "Grain boundary slip transfer classification and metric selection with artificial neural networks", Scripta Materialia **185**, 71 (2020).

[199] H. Zheng, X. G. Li, R. Tran, C. Chen, M. Horton, D. Winston, K. A. Persson, and S. P. Ong, "Grain boundary properties of elemental metals", Acta Materialia **186**, 40 (2020).

[200] B. Zhou, Y. Li, L. Wang, H. Jia, and X. Zeng, "The role of grain boundary plane in slip transfer during deformation of magnesium alloys", Acta Materialia **227**, 10.1016/j.actamat.2022.117662 (2022).

[201] B. Zhou, L. Wang, P. Jin, H. Jia, H. J. Roven, X. Zeng, and Y. Li, "Revealing slip-induced extension twinning behaviors dominated by micro deformation in a magnesium alloy", International Journal of Plasticity **128**, 102669 (2020).